Lakehead University

Prediction of overheating close to bone interfaces generated by high intensity ultrasound transducers

Sandra Diaz

A thesis submitted for the degree of
MsEng in Electrical and Computer Engineering
July 2013

Contents

List of Figures

List of Tables

Abreviations

ASM	Angular Spectrum Method
BEM	Boundary Element Method
BHTE	Bio heat transfer equation
CUDA	Computer Unified Device Architecture
FEM	Finite Element Method
FOV	Field of view (MRI)
GPU	Graphic Processing Unit
HIU	High intensity ultrasound
MRI	Magnetic resonance imaging
PRFS	Proton resonant frequency shift
TE	Echo time (MRI)
TR	Repetition time(MRI)

Symbols

c	Speed of sound
p	Acoustic pressure
R	Distance between a source point and a point in the medium
t	Time
T	Temperature
v	Particle velocity
Z_l	Longitudinal specific impedance
Z_t	Transversal or shear specific impedance
α	Acoustic attenuation coefficient
β	Acoustic absorption coefficient
γ_1	Shear refraction angle
κ	Wave number
λ	Wavelength
ρ	Density
θ	Incidence and reflection angle
θ_1	Longitudinal refraction angle

Abstract

One of the driving forces for research in medical sciences is to develop more effective and less intrusive treatments. High Intensity Ultrasound (HIU) is a technique that uses the acoustic field produced by a transducer to induce thermal effects in soft tissue for therapeutic purposes like tissue ablation for cancer treatment, localized drug delivery, sonoporation, among others. The bioeffects induced in soft tissue by HIU, particularly close to solid (bone) interfaces, are not yet fully understood. The objective of this thesis work is to gain further understanding of the effects that the waves reflected by bone have on the treatment outcome.

This study presents the experimental validation of a simple and efficient method to calculate the acoustic field generated by a high intensity ultrasound (HIU) transducer that is used in the vicinity of a solid interface. The model takes into account the interaction between the forward and the reflected wave generated at the boundary between a fluid and a solid. It uses a modified Rayleigh-Sommerfeld integral to calculate the particle displacement over a reflecting surface and uses the particle displacement at the boundary as a new acoustic source to obtain the reflected particle displacement. The thermal effect of the acoustic field is finally calculated using the bio heat transfer equation (BHTE) accounting for both the forward and the reflected waves.

Simulations using the proposed method were compared against exper-

imental data of acoustic pressure acquired using a 0.075-mm needle hydrophone and a 7.29 MHz ultrasound transducer. A solid reflector was placed at different incidence angles (0, 5 and 10°) and experimental scans were compared to simulations. The average absolute error between simulation and measurements was 3.9% ± 0.54%, 8.18% ± 0.79% and 7.23% ± 0.47% for 0°, 5° and 10° incidence angles respectively.

Thermal effects were studied using a spiral-shaped tissue-mimicking phantom heated with an interstitial device placed and rotated at its centre to target a cylindrical region around it. The device was a rectangular planar transducer with 3 active 4x5-mm elements operating at 4.58 MHz. The spiral-shape phantom recreated the scenario where bone tissue gets closer to the ultrasound device as it rotates. Magnetic resonance-based thermometry was acquired on a Philips Achieva 3T MRI scanner during heating using a T1-based thermometry sequence (TE = 15 ms, TR = 90 ms, FOV= 160x160x25 mm, Slice thickness = 5 mm, 5x1x1 mm voxel, 5.1 s frame rate, α = -0.0095 ppm/°C , baseline temperature = 22°C). Thermal maps were then compared to the predicted thermal effects obtained using the BHTE. The comparison between the experimental measurements and the simulations indicated that the model predicts with good accuracy the temperature increase generated by the ultrasound transducer facing a solid interface. The results showed that considering the wave reflected at the boundary increased the accuracy of thermal calculations, since without this wave the error can be as high as 30%.

This model can provide with an accurate and fast calculation of temperature increases for HIU therapeutic applications where the devices are used in proximity to bone interfaces.

Acknowlegdements

I would like to thank my supervisor Dr. Samuel Pichardo and my co supervisor Dr. Laura Curiel for the invaluable opportunity they gave me to come to Canada and study under their guidance; for their support, mentorship and friendship. I would like to thank also Dr. Ehsan Atoofian, Dr. Mark Gallagher and Dr. Oleg Rubel for their valuable comments on my thesis work. I would also like to thank Dr. Rajiv Chopra for his support and valuable feedback and all my friends inside and outside the Thunder Bay Regional Research Institute for sharing their advise and perspectives on my work.

I would like to thank my family, because without their endless support I would have not been able to complete my studies and specially to my dear son Aaren who embarked with me in this adventure and has been my support, companion and motivation.

Simulations for this thesis work were performed on hardware donated by NVIDIA Corporation (Santa Clara, CA, USA). This project was supported by the RBC Royal Bank Mark Poznansky Student Mentorship Award and partially funded by the Ontario Research Fund Round 2. I would also like to thank Ritesh Patel for providing us the datasets for the MRI thermometry experiments used in this thesis.

Chapter 1

Introduction and Motivation

One of the driving forces for research in medical sciences is to develop more effective and less intrusive treatments. High Intensity Ultrasound (HIU) has been proposed as a minimally intrusive technology for cancer treatment. HIU was first conceptualized in the 1940s (Lynn et al. 1942) but its usage in medical applications was heavily delayed by the lack of monitoring techniques which could help confirm and guide the treatments (Damadian 1974). The introduction of magnetic resonance imaging (MRI) medical imaging technologies in the clinical field during the last twenty years allowed the development of new image-guided HIU applications

HIU is a technique that uses the acoustic field produced by a transducer to induce thermal effects in soft tissue for therapeutic purposes (see figure 1.1). It is well suited to induce thermal effects in the proximity of the device. These transducers can be embedded into small applicators with integrated cooling (Diederich 1996) in order to access regions which are difficult to treat while being minimally invasive (Lafon et al. 1998). Some applicators have been specifically built to be MRI-compatible and target tissue volumes by performing small cumulative lesions using rotational controllers (Ross et al. 2004). This allows for MRI guidance and real-time feedback of

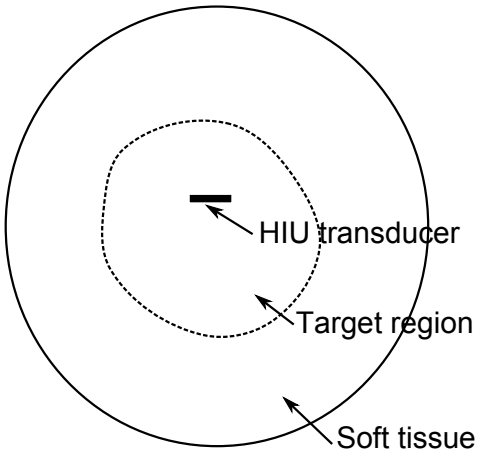

Figure 1.1: Diagram of a HIU interstitial device inserted in soft tissue (top view). The dotted line defines the therapy target region around the transducer.

the thermal effects of the treatment, thus ensuring that the target regions are ablated properly and in a confined manner. As the target regions for HIU applications become more complex in composition, shape and location, simulations of the physical effects of exposing the target tissue to ultrasound become essential to ensure the safety and efficiency of the treatments (NDjin et al. 2012, Miller et al. 2012).

The bioeffects induced in soft tissue by HIU, particularly close to solid (bone) interfaces, are not yet fully understood. The objective of this thesis work is to gain further understanding of the effects that the waves reflected by bone have on the treatment outcome. This knowledge will be valuable in assisting treatment planning, transducer design and treatment control to ensure the safety and efficiency of the procedures. To achieve this goal, this study proposes a precise, yet computationally efficient, method to model the acoustic pressure field close to a solid interface and asserts that it can accurately predict increments in temperature caused by the interactions between

the forward and reflected waves close to solid boundaries. The method is based on the Rayleigh-Sommerfeld integral (Pierce 1994) and considers the forward wave produced by the acoustic source combined with the reflected wave produced by a solid interface. This model is an extension to previous work for the calculation of the transmitted pressure of shear and longitudinal waves into bone (Pichardo & Hynynen 2007). The accuracy of the model was validated by comparing simulations to pressure measurements of the forward and reflected wave at different angles of incidence. Then, the thermal effects induced by the combined forward and reflected waves was calculated and compared to experimental magnetic resonance-based thermometry on a tissue phantom.

This thesis is divided as follows: therapeutic applications of HIU will be explored in chapter 2. In chapter 3, a review of the theoretical background of the method and current modelling techniques will be discussed. In chapter 4, an experimental setup to measure the acoustic field produced close to solid interfaces will be presented along with the method proposed to model this phenomenon. Implementation and simulation details will also be discussed and finally, the results of validating the proposed method against experimental measurements will be summarized and commented. Chapter 5 introduces an experimental setup to measure thermal effects induced by a HIU transducer on a tissue-mimicking phantom, as well as the implementation of a strategy to model these effects using the calculated acoustic field in combination with the Bio Heat Transfer Equation. Results of validating the simulations against the experimental data will also be discussed. Finally, in chapter 6, the main contributions of this study will be discussed and conclusions will be provided.

Chapter 2

High Intensity Ultrasound therapeutic applications

In order to utilize ultrasound as a therapeutic tool, it is necessary to create devices that generate ultrasonic waves and enable the propagation of those waves into tissue. Ultrasound is generated using the piezoelectric effect. Ultrasound transducers made of piezoelectric materials can be exposed to an electric field to produce a mechanical deformation. Piezoelectric materials behave as mechanical springs and the displacement of the transducer's surface is directly proportional to the stress applied to it (Hunt et al. 1983). Materials commonly used for this purpose are quartz crystals and lead zirconate titanate (PZT). The material used to build the transducer dictates the way it responds to electric excitation as well as its capability to transform electrical energy into mechanical energy. Ultrasound transducers can also be used to transform mechanical vibrations into an electric signal which is the principle used for imaging.

When ultrasound propagates through tissue, the variations in pressure induce motion which leads to frictional heating. This means that a portion of the mechanical energy carried by the acoustic wave is turned into heat by

viscous absorption. This phenomenon is used to produce tissue heating and is one of the most widely used therapeutic effects of ultrasound. An ultrasound wave also scatters as it propagates through mediums with different acoustic characteristics. The loss of acoustic energy in a medium can be accounted for as the sum of its absorption and scattering coefficients. This is quantified by the attenuation coefficient which is related to the frequency of the ultrasound wave by

$$\alpha = af^b, \tag{2.1}$$

where a and b are constants specific to each type of tissue. A higher frequency yields a higher attenuation and higher energy absorption but lower penetration depth (ter Haar & Coussios 2007).

Based on the bio-effects produced by high intensity ultrasound, several therapeutic applications have been proposed in the past years including: localized sonophoresis for drug delivery, physical therapy of muscle and joint disease, sonoporation and tissue ablation for cancer treatment. All these effects have been studied to define therapeutic parameters for each application depending on the position of the target tissue. These parameters include: element size and frequency of the transducer, exposition time of tissue to the ultrasound wave and motion of the acoustic field to generate cumulative lesions.

The technique used for localized thermal drug delivery, especially through the skin, using ultrasound is called sonophoresis (Bommannan et al. 1992). Sonophoresis is used to enhance the permeability of the skin and allow low molecular weight drugs as well as macromolecules to be delivered to or through skin. Ultrasound waves are used to stimulate microvibrations in the epidermis, creating small openings in the skin which allow fluids to travel in or out the body. It can also be used to perform non invasive control of

blood sugar for diabetics, by performing short term or long term delivery of insulin (Parakka 2013).

Localized drug delivery can also be achieved by encapsulating molecules inside liposomes which release their content when they interact with ultrasound. This phenomenon does not rely on heat, but on the capsule opening under the external pressure exherted by the wave (Huang et al. 2008).

Sonoporation is the effect of generating pores in the cell membrane using ultrasound and microbubbles. This technique enhances the permeability of the cells and the inward transport of molecules which otherwise would be unable to cross the membrane. Sonoporation is based on a mechanically induced bio effect of ultrasound exposure of the cell membrane to cavitation. Sonoporation is in its early stages of development but promises great results for non invasive in vivo nonviral gene therapy and localized drug delivery (Bao et al. 1997, Miller et al. 2002, Pan et al. 2005).

An area of high interest for HIU is oncology. Cancer care has found in HIU a minimally invasive, radiation free alternative for palliative and treatment purposes. In the next section, special focus will be given to HIU applications for cancer treatment.

2.1 Cancer treatment

Standard therapy for cancer encloses the following options depending on the type and region to be treated and overall health of the patient:

- Surgery is used for diagnosis and treatment based on full or partial resection (Cohen et al. 2013). Age and overall health of the patient as well as the location of the tumour are important variables to consider.

Side effects include complications due to the intervention, anaesthetics, risk of infection and long recovery time among others.

- Radiation therapy can be used for curative or palliative purposes (Walker et al. 2013). It is more cost effective and provides better life expectancy than surgical resection (Vuong et al. 2013) but treatment close to high risk structures is challenging and secondary effects such as radiation of normal tissue have to be considered.

- Chemotherapy provides medication to stop or slow the growth of tumour cells. It works on rapidly dividing cells by causing damage to their DNA and preventing cell repair. Side effects of chemotherapy include nausea and vomiting, skin reactions, alopecia, otitis, fatigue and somnolence (McNamara 2012).

- RF ablation works by inducing thermal effects using micro-wave antennas. A localized heating pattern can be achieved without overheating surrounding normal tissues. It mitigates invasiveness and side effects when compared to other alternatives, leading to improved quality of life. The heating pattern generated using the antenna is difficult to control in order to ablate complex shapes (Kikuchi et al. 2007, Takahashi et al. 2006, Sheta et al. 2012).

When other alternatives prove to be ineffective or difficult to apply due to the position, size or accessibility to the tumour region, HIU therapy can be used as an alternative. In some circumstances techniques like radiochemotherapy and laser photocoagulation are ineffective and expensive (Melodelima et al. 2003). Some tumours can be difficult to treat because they have variable thickness and complex shape, or due to their extent at diagnosis and presence of comorbidity. HIU is capable of ablating tissue within irregular volumes and can be used in combination with other treatments because it is drug and radiation free. By selecting different operating frequencies and power for the transducer's elements, better control on the depth and

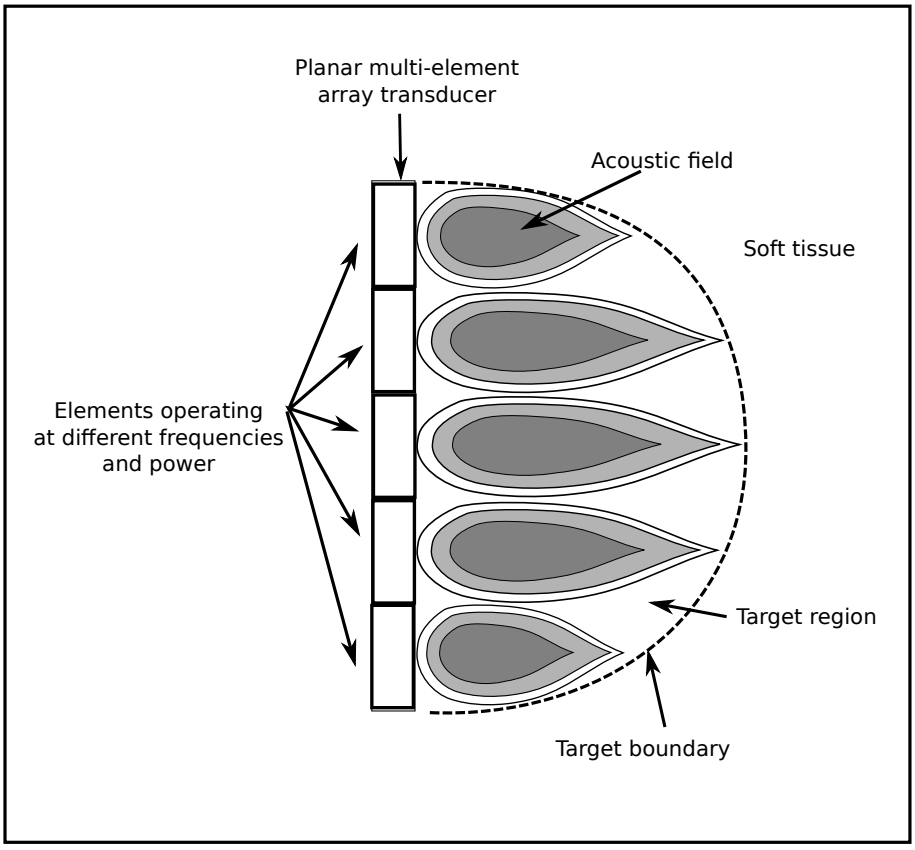

Figure 2.1: Diagram showing a planar transducer with multiple elements for which individual frequencies and power values can be specified.

shape of the volume of ablated tissue around the device can be achieved (see figure 2.1). Thus, HIU can be used to induce cellular necrosis targeting deep tissue while remaining minimally invasive and provide conformal treatment. HIU has been proposed as an alternative for the treatment of localized cancer in organs such as prostate (Chopra et al. 2008), brain (Canney et al. 2010), cervix (J H Wootton & Diederich 2011) and liver (Delabrousse et al. 2010).

A relevant area of study in HIU revolves around asserting the feasibility of performing conformal thermal ablation and creation of controlled and reproducible heating patterns to ensure safety and efficiency of the treatments. Inhomogeneities in the propagating material cause sound to reflect and refract as it propagates through it. When differences in the acoustic properties of the materials are high, i.e. between muscle and bone, these distortions become more prominent. HIU therapy requires careful treatment planning to ensure that heat deposition will be performed in such a way that enough energy is delivered to induce thermal coagulation but only within the desired target region. Software has also been developed to simulate the effects of ultrasound propagation in tissue using anatomical information of the patient obtained using CT scans (Aubry et al. 2003, Tanter et al. 2007, Wein et al. 2008, Kutter et al. 2009*a*). This allows a more realistic prediction of the procedure's outcome.

For example, the brain has been extensively studied for ultrasound thermal treatment removing the skull but other alternatives which aim to keep the skull intact or almost intact have to deal with the high absorption coefficient and reflections induced by the skull (Hynynen & Sun 1999, Tanter et al. 2007). One approach is to use a HIU interstitial device which is inserted in the brain through an incision made in the skull. Experiments on ex vivo bovine and sheep tissue using MRI temperature monitoring and lesion characterization, as well as comparisons with mathematical models under

this approach have been presented in (Canney et al. 2010). This method poses an alternative treatment for brain tumours without removing the skull and eliminates the need of the ultrasound beams to travel through the skull to reach the target region. Nevertheless, accurate prediction of the deformations of the acoustic field caused by the ultrasound waves reaching the interface between the brain and the inner wall of the skull is still fundamental to ensure that tissue beyond the treatment area is kept unharmed.

As another example, J H Wootton & Diederich (2011) show in their work a study of endocervical and interstitial tubular HIU transducers used in combination with brachytherapy to treat cervical cancer. Given the inhomogeneous tissue properties in the region, the variable blood perfusion and the possibility of inducing thermal toxicity to the rectum and bladder, treatment in the region requires considerable planning and analysis. The authors use a treatment planning tool based on a Finite Element Method to simulate tissue heating in 3D models acquired using CT scans or high resolution MR images and analyse different configurations for the positioning of the devices and achieve the desired effects for therapy. An important conclusion in their work is that directional control of energy delivery and treatment planning are critical to ensure therapeutic thermal coverage without overheating neighbouring anatomical structures.

HIU treatment safety and efficiency applied to the prostate gland has been extensively studied. Special attention will be given to this application in the following section.

2.1.1 Prostate treatment

Devices and methodologies for prostate gland ablation with MR-guided HIU have been proposed in the past years (Siddiqui et al. 2010, Diederich et al. 2004, Chopra et al. 2004.) and its feasibility for human use has been asserted

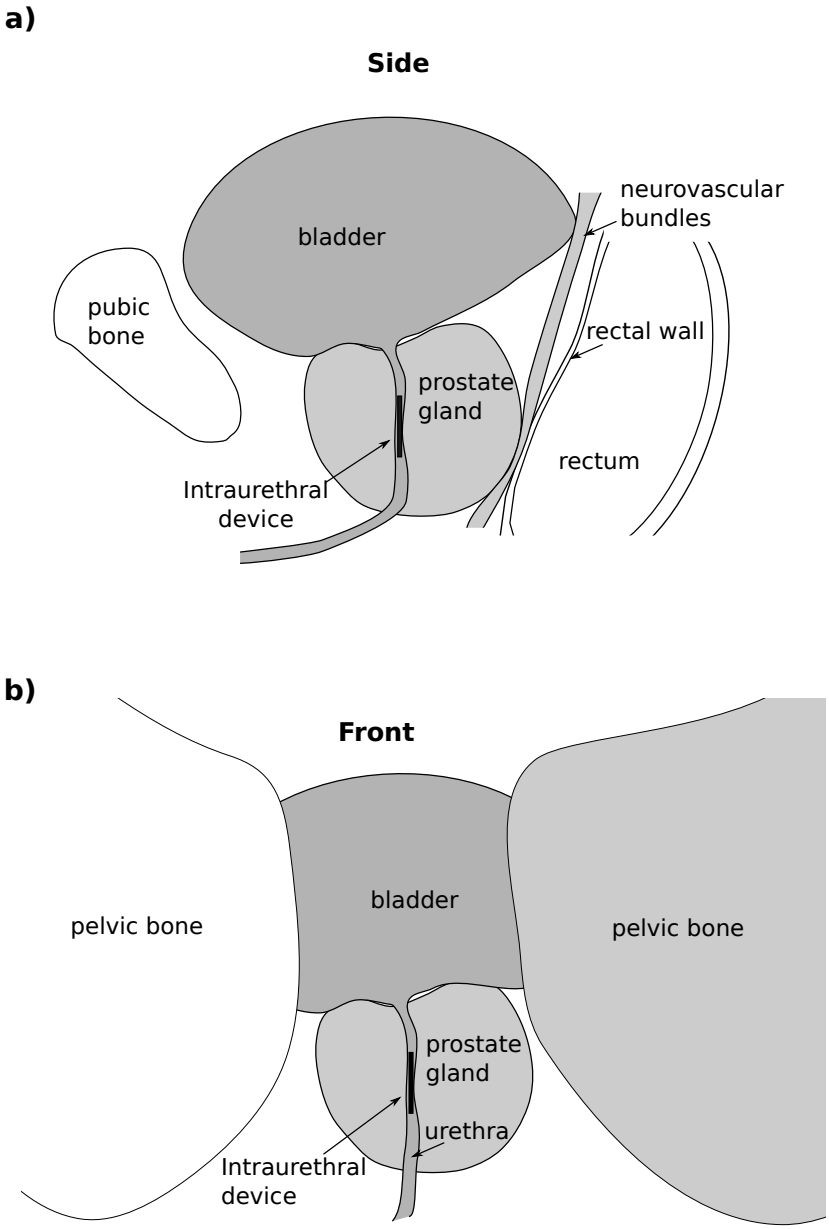

Figure 2.2: Diagram of a HIU intraurethral device for prostate gland ablation.

(Chopra et al. 2012). The prostate region shows several challenges for the accurate and safe ablation of the organ because of its difficult to access location, proximity to the pelvic bone and the inhomogeneities of the surrounding tissue (figure 2.2). Burtnyk et al. (2010), performed a thermal analysis concluding that it is possible to ablate the whole volume of the prostate but strategies must be developed to avoid causing thermal injury to the rectum, pelvic bone, neurovascular bundles and urinary sphincters and included in any appropriate treatment planning. Their results show that when the target regions are close to the pelvic bone (in their case, closer than 10mm when using a 4.7MHz transducer), significant heating of this bone and neighbouring tissue outside the target area is produced.

The study described by NDjin et al. (2012) also highlights the importance of performing simulations to ensure treatment safety when targeting tissue close to the bone. Here, the authors performed simulations and heating experiments on gel phantoms using 3D anatomical models of the human prostate to define the target volumes. Their objective was to identify the considerations required to ablate the whole prostate volume while ensuring safety and efficiency of the treatment. Among their conclusions, the authors mention that using multiple frequencies during treatment is important to create accurate heating patterns confined to the desired target region and avoiding undesired overheating of tissue close to the bone (figure 2.3). This means that multiple frequencies are required not only to generate lesions of arbitrary shapes but also to ensure that neighbouring tissue to structures such as bones are not overheated.

In order to ablate complex shaped tissue volumes around the device, different approaches have been taken. The form of the transducer has a direct impact in the distribution of the acoustic field around it and thus, in the shape of the volumes that can be treated as well as in the accuracy that can

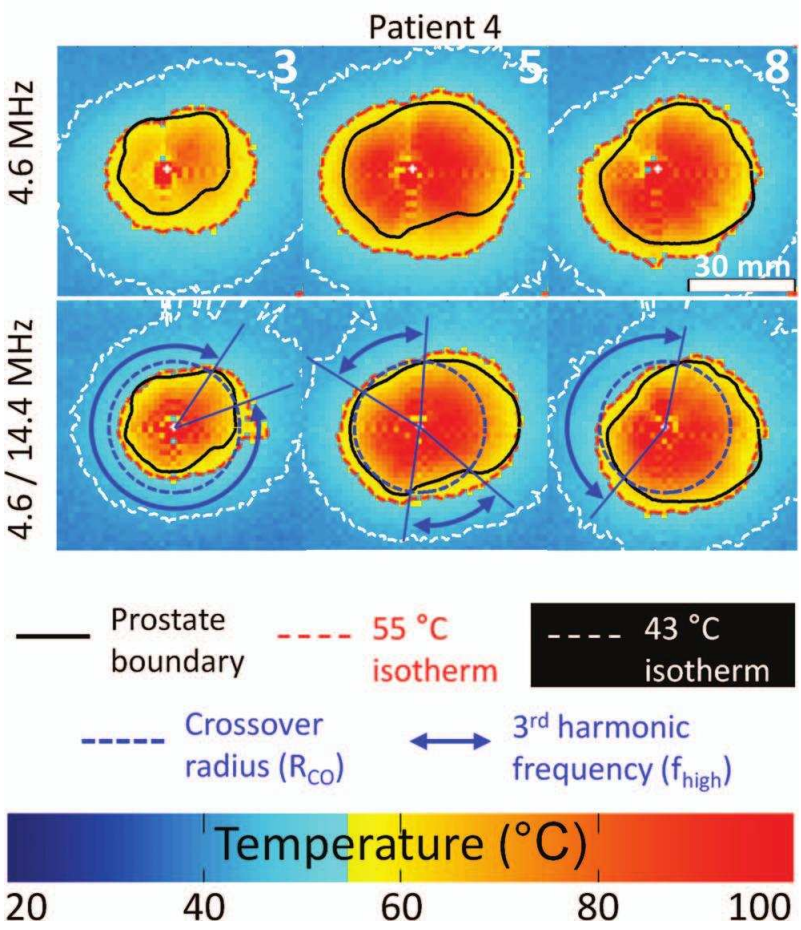

Figure 2.3: Image illustrating the benefits of using multiple-frequency devices in the ablation of full human prostate volumes (NDjin et al. 2012). Heating of a gel phantom using a transducer operating at the fundamental frequency of 4.6MHz was compared to heating performed with a transducer operating at the fundamental frequency of 4.6MHz and the 3^{rd} harmonic frequency of 14.4MHz. A crossover radius was defined such that if the radius of the prostate for that section was smaller, the 3^{rd} harmonic frequency was used. This technique enhanced the radial targeting accuracy by a factor of 30%.

be achieved. Multi-sector tubular (Kinsey & Diederich 2008, J H Wootton & Diederich 2011, Ross et al. 2004) and planar transducer (Lafon et al. 1999, NDjin et al. 2012) arrays have been proposed either working at single or multiple frequencies (Burtnyk et al. 2010).

Two main types of applicators have been proposed for the ablation of the prostate gland: interstitial (transurethral) and transrectal, the later working with focused transducers. Interstitial applicators with planar transducers operating at multiple frequencies provide the ability to control lesion depth by selecting the appropriate power and frequency. Interstitial devices offer direct path to the prostate using a transurethral access while being minimally invasive, but pose the challenge of delivering enough energy to ablate the whole gland while sparing the surrounding anatomy (R Chopra & Bronskill 2005.). Ex-vivo heating experiments performed by Chopra et al. (2000), confirmed the ability to create arbitrary lesion geometries during heating using a multi-layered transducer for interstitial thermal therapy. The radius of the lesion was controlled by varying the scan rate or exposure time and the frequency. Lesions produced using the proposed device were continuous and conformal which is of high importance for treatments close to important anatomical structures.

In Chopra et al. (2004.), the authors perform a numerical study of a control technique to apply HIU to the prostate by varying the frequency and exposure time of the treatment device (a single planar transducer with two operating frequencies) during heating. Their method allowed them to simulate the ablation of 3D volumes generated from clinical MR images of the prostate with an accuracy of 3mm. They used a simulation of the acoustic field based on Raleigh-Sommerfeld integral (see section 3.1.4) and a finite difference solution of the bio heat transfer equations (see section 3.2) to control the power, scan rate and frequency of the treatment device. Rectal cooling

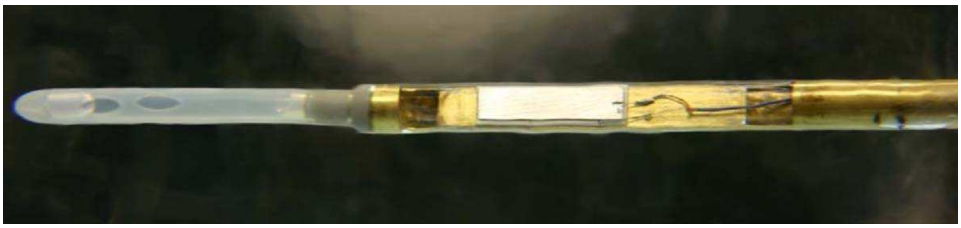

Figure 2.4: Interstitial applicator proposed in (Chopra et al. 2008).

was proposed to protect the rectal wall from undesired overheating. This approach is similar to the one followed in the thermometry validation experiment presented in this thesis work.

The development of MRI compatible HIU devices has been fundamental in the generation of clinically viable therapy proposals which incorporate real time feedback of the treatment outcome and help avoid undesired side effects. First in-vivo evaluations of MRI guided therapy (Hazle et al. 2002, Diederich et al. 2004) proved that thermal maps obtained using Magnetic Resonance Temperature Imaging (MRTI) correlated well to actual thermal doses being applied. For these studies, the authors designed an applicator incorporating multiple tubular transducers with 180° sectors and a frequency between 7 - 8 Mhz, with which it was possible to ablate relatively large portions of the prostate gland (180° with a depth of 1.5 - 2 cm from the urethra) in reasonable times (between 10 and 15 minutes). The applicator included a cooling balloon which was inflated to maintain the position of the device during the procedure as well as to provide coupling and cooling of the tissue in immediate vicinity to the urethra. Cooling was performed by running degassed water through the balloon with a flow rate of 80-100 ml/min at 22° C. With these studies, it was noticed that directional applicators with rotational capabilities would be highly useful to ablate the prostate in a more controlled and confined manner.

Figure 2.5: MRI-compatible positioning system and rotational motor attached to the heating applicator (Chopra et al. 2008).

Ross et al. (2004) evaluated the performance of 90° sectored tubular transducers and planar transducers combined with a manual rotational control for MRI guided prostate ablation. The authors concluded that tubular transducers are more suitable to induce necrosis in tissue closer to the urethra in short time while sparing neighbouring structures. Planar transducer are better for deeper and more complex shaped targeting. MRI compatible rotational control enhanced the accuracy of heat deposition.

Chopra et al. (2008) showed the feasibility of using MRI compatible interstitial devices and automatic rotational controls to perform therapy delivery and MRI thermal monitoring at the same time. In the study, a series of heating experiments were performed on gel phantoms and a canine model. The devices and controls used in these experiments, shown in figures 2.4 and 2.5, achieved precise patterns of thermal damage in the target tissue with almost real time feedback of the temperature variations. The method used to obtain the temperature scans with the MRI in all the previously mentioned studies was proton resonant frequency shift (PRFS) which is the same method used in the thermometry validation section of this thesis (Rieke & Pauly 2008).

In conclusion, a variety of applications have been considered to apply the bio-effects produced by high intensity ultrasound for therapeutic purposes. Among its more relevant application s we find thermal effects for tissue coagulation. Proper understanding of the way ultrasound propagates through inhomogeneous tissue is essential to ensure the safety and efficiency of the procedures. For this purpose, treatment planning tools, real time monitoring and controls should be developed. The effects of targeting tissue close to bone interfaces remains an open area of study and adequate modelling of this phenomenon will be relevant for treatment planning and transducer design in the near future.

Chapter 3

Modelling for High Intenstity Ultrasound applications

Using HIU over inhomogeneous tissue brings additional complexity to treatments as the acoustic field generated by the transducer is deformed at the interfaces between tissues with different acoustic properties. When the difference between the acoustic impedance of the materials is high (as in the case of soft tissue and bone interfaces), reflections and refractions distort the pressure distribution. To ensure safety and efficiency during treatment, computational models are required to predict these changes depending on the treatment requirements.

3.1 Modelling of the acoustic pressure field

3.1.1 The wave equation

The wave equation is the fundamental equation of acoustic propagation in a dissipative fluid medium. It is derived from the conservation of mass equation and Euler's equation of motion (see Pierce (1994), Brekhovskikh & Godin

(1998) and Bruneau & Scelo (2006) for details on the following derivations).

For a particle within a fluid with a fixed volume, the equation for the conservation of mass is given by

$$\frac{\partial \rho}{\partial t} + \bigtriangledown \cdot (\rho v) = 0, \tag{3.1}$$

where ρ is the density of the medium, t is time and v is the fluid particle velocity.

Euler's equation is given by

$$\rho \frac{Dv}{Dt} = - \bigtriangledown p, \tag{3.2}$$

where the term $Dv/Dt = \partial v/\partial t + v \cdot \bigtriangledown v$ represents the time rate of change in velocity of a fluid particle as measured at the fluid particle, and p is pressure exerted over the fluid particle (Pierce 1994). This equation is an expression of Newton's second law of motion where the left portion is the mass of the fluid particle times the acceleration and the right hand represents the total apparent force per unit of volume caused by spatial variations of the pressure.

If v_0, p_0 and ρ are defined as the undisturbed particle velocity, pressure and density and v', p' and ρ' as disturbances of these properties caused by the presence of a sound wave, the sum of these quantities $\hat{v} = v_0 + v'$, $\hat{p} = p_0 + p'$ and $\hat{\rho} = \rho_0 + \rho'$ obey the thermodynamic equations of conservation of mass and Euler described above as well as the state equation $p = p(\rho, s)$, where s is the specific entropy of the particle (Pierce 1994).

After neglecting second or higher-order terms, the following set of linear equations is obtained:

$$\frac{\partial \rho'}{\partial t} + \rho_0 \bigtriangledown \cdot v' = 0, \tag{3.3}$$

$$\rho_0 \frac{\partial v'}{\partial t} = - \bigtriangledown p', \tag{3.4}$$

$$p' = c^2 \rho' \tag{3.5}$$

with

$$c^2 = (\frac{\partial p}{\partial \rho})_{s=0}, \tag{3.6}$$

where c is the speed of sound in the medium.

The wave equation is derived from the linear acoustic equations above, and is given by

$$\bigtriangledown^2 p - \frac{1}{c^2} \frac{\partial^2 p}{\partial t^2} = 0, \tag{3.7}$$

where the operator $\bigtriangledown^2$ is the laplacian sum of second derivatives with respect to the three cartesian coordinates. The form of this equation suggests that sound is a wave phenomenon as its solutions adhere to the notion of a wave traveling as a disturbance with neglectable amount of matter transport through a medium.

The wave equation 3.7 can be solved for the case of a plane traveling wave with acoustic field varying only with respect to time and one cartesian coordinate d while being the same along normal planes to the propagation

direction. The solution for the wave equation is then

$$p = f(t - \frac{1}{c}d), \tag{3.8}$$

where f is an arbitrary function.

If the acoustic disturbance is a wave with a single frequency, the field oscillates sinusoidally over time so the pressure can be expressed as

$$p = p_{pk}\cos(\omega t - \phi) = Re[\hat{p}e^{-i\omega t}], \tag{3.9}$$

where p_{pk} is the peak pressure, ω is the angular frequency, $\hat{p}$ is the complex pressure amplitude and ϕ is the phase constant. The latter expression is used to replace the amplitude and phase by a single complex number. Substituting this expression into the linear acoustics equations, allows the transformation of the wave equation into the Helmholtz equation

$$\bigtriangledown^2\hat{p} - \kappa^2\hat{p} = 0, \tag{3.10}$$

where κ is the wave number ω/c.

Another possible solution would be that of an spherical wave where all acoustic field variables depend now on time and a radial distance r from the source. For this scenario, the wave equation turns into

$$\frac{1}{r}\frac{\partial^2}{\partial r^2}rp - \frac{1}{c^2}\frac{\partial^2 p}{\partial t^2} = 0, \tag{3.11}$$

Considering only waves moving radially away from the source, then the solution for the wave equation has the form

$$p(r,t) = \frac{1}{r}f(t - \frac{1}{c}r), \tag{3.12}$$

where f again is an arbitrary function.

3.1.2 Point sources and Green equations

A spherically symmetric source with angular frequency ω within an unbounded fluid has the following complex pressure amplitude

$$\hat{p} = \hat{S}\frac{exp(i\kappa R)}{R}, \tag{3.13}$$

where $\hat{S}$ is the monopole amplitude and $R = x - x_s$ is the distance between the source(x_s) and a point in the fluid (x).

This field satisfies Helmholtz equation everywhere except close to the source, which can be expressed as

$$(\bigtriangledown^2 + \kappa^2)\hat{p} = -4\pi\hat{S}\delta(x - x_s), \tag{3.14}$$

where $\delta(x - x_s)$ is the Dirac delta function.

The solution of equation 3.14 with $\hat{S} = 1$ is the Green's function $G_k(x|x_s)$ that satisfies

$$(\bigtriangledown^2 + \kappa^2)G_k(x|x_s) = -4\pi\delta(x - x_s). \tag{3.15}$$

Here, $G_k(x|x_s) = R^{-1}e^{i\kappa R}$ if the fluid outside is unbounded. Using the superposition theorem, Green's functions can be used to generate solutions considering several point sources.

For N source points, the complex acoustic pressure amplitude obeys Helmholtz equation as a sum of source terms $-4\pi\hat{S}_n\delta(x - x_n)$ on the right side of the equation, resulting in

$$\hat{p} = \sum_{n=1}^{N} \hat{S}_n G_k(x|x_n). \tag{3.16}$$

3.1.3 The Kirchhoff-Helmholtz integral

The Kirchhoff-Helmholtz integral theorem (Kirchhoff 1883, Helmholtz 1860) expresses pressure at a point inside or outside a surface S in terms of the

pressure and particle velocity values at that surface. It is derived when one considers a surface enclosing a source within an unbounded fluid. Using the free space Green's function one can express the source as being a sum of source points and obtain the expression for the Kirchhoff-Helmholtz integral which is given by

$$\begin{aligned} p(x,t) = & \frac{\rho}{4\pi}\int\int \frac{v_n(x_S, t-R/c)}{R} dS \\ & + \frac{1}{4\pi c}\int\int e_R \cdot n_S (\frac{\delta}{\delta t} + \frac{c}{R}) \frac{p(x_S, t-R/c)}{R} dS \end{aligned} \tag{3.17}$$

where $R = |x - x_S|$, $e_R = (x - x_S)/R$ and n_S is the unit normal to S pointing out of the surface.

3.1.4 Rayleigh-Sommerfeld integral

The Rayleigh-Sommerfeld integral is an special case of the Kirchhoff-Helmholtz integral where a flat source of varying thickness is considered to be in an unbounded fluid. The normal velocity v_n on both sides of the plate has the same value (either moving outwards or inwards simultaneously) so p, v_x and v_y are even but v_z is odd. Consequently the integral over the surface pressure give equal and opposite contributions, and the net contribution over the surface pressure to the Kirkhoff-Helmholtz integral is zero. The integral over the surface normal velocity from front and back of the surface of the disk give equal contributions, so one need only to integrate over one side and multiply the resulting expression by 2. As a result, the Kirchhoff-Helmholtz integral turns into the Rayleigh-Sommerfeld integral given by

$$p(x,t) = \frac{\rho}{2\pi}\int\int \frac{-i\omega \dot{v}_n(x_s) e^{i\kappa R}}{R} dx_s dy_s \tag{3.18}$$

3.1.5 Numerical Methods and simulations

Numerical methods, such as the numerical implementation of the Rayleigh-Sommerfeld integral, the finite element (Lerch et al. 1992, Lerch et al. 1994), the boundary element and the angular spectrum methods (Vyas & Christensen 2008, Wu & Stepinski 1999, Zeng & McGough 2008), can be used to efficiently and accurately describe the propagation of acoustic waves in homogeneous and heterogeneous environments. This thesis presents a method to calculate the acoustic field close to an interface, where the interactions of forward and reflected waves are the center of interest. The methods detailed in the following section have been developed for the simulation of stationary waves and neglect non linear effects.

Numerical implementation of the Rayleigh - Sommerfeld integral

The Rayleigh-Sommerfeld integral has been used in the past to reliably model acoustic fields in homogeneous media. As explained in section 3.1.4, this technique considers that the pressure at each point can be calculated as the sum of the contributions of an infinite number of elements which form the acoustic source. Its numerical implementation considers that the source is divided into a finite number of smaller elements and the propagation medium is discretized into a grid of points where the pressure is calculated. To ensure reliability of the method, in both the source and the propagation space, the discrete points must not be separated by more than half the wave length used. If implemented as a serial process, the algorithm is computationally expensive. However, the integral is highly parallelizable as the calculations at each point are independent from each other. Rayleigh-Sommerfeld integral is the start point for other approaches for the calculation of the acoustic pressure field such as the Angular spectrum method. It has also been used as benchmark to assess the performance of other numerical methods.

Angular spectrum methods

The angular spectrum (ASM) approach describes the diffraction of acoustic waves by representing an acoustic wave as a superposition of plane waves traveling in different directions and then propagating these components in the spatial frequency domain. The method allows the diffractive propagation of any harmonic field between two arbitrarily distant parallel planes to be treated as the propagation of planar waves between the same planes. The angular spectrum method can work with the particle velocity or the pressure values at the source.

The two dimensional Fourier transform of a harmonic field in a plane is equivalent to a decomposition of the field in a sum or harmonic plane waves traveling over a spectrum of angles. This sum of harmonic waves is called the angular spectrum of the field. Equation 3.18 is actually a 2D convolution that can also be expressed in this form

$$p(x, y, z, t) = j\rho cke^{j\omega t}u(x, y) \bigotimes h_u(x, y, z),$$

where the spatial propagator $h_u(x, y, z)$ is given by

$$h_u(x, y, z) = \frac{e^{-jkr}}{2\pi r},$$

where, r is the distance from the origin to an arbitrary field point (Zeng & McGough 2008).

The angular spectrum method consists of a series of steps to obtain the pressure field at a target z plane. First, samples from the source function are acquired. The second step is to transform the sampled source function points using a discrete henkel transform (DHT) or a 2D fast fourier transform

(FFT). (Zeng & McGough 2008) proposed two ways to perform the next step. One way is to sample the propagation function and transform the sampled function points using again a DHT or 2D FFT. In the second alternative, the propagation function can be first transformed and then samples of it can be taken in the spatial frequency domain, which can be easily be extended to work with multilayer propagation in complex, inhomogeneous mediums and produces similar results but is more susceptible to errors when the right sampling method is not used. The fourth step is to multiply the source and the propagation functions in the spatial frequency domain. The final step is to calculate the inverse transform on the resulting values of the last step to go back to the spatial domain and obtain the desired complex field results.

An extension of the ASM to treat inhomogeneous, complex mediums was introduced in (Vyas & Christensen 2012, Vyas & Christensen 2008) and is called hybrid angular spectrum. In this method the space is discretized into voxels. Each voxel can have different acoustic properties. Then the voxels are consolidated into planes. The normal ASM is performed for each plane and the output of one is used as input for the next plane. This method is efficient, relatively fast and can work with complicated shapes and inhomogeneous mediums.

Finite element and boundary element methods

The finite element method (FEM) is an approach which is widely used in engineering. For acoustic modelling using FEM, the propagation space is discretized into small volumes of variable shape and size, which makes it a very versatile method to do calculations within irregular volumes. Then a set of base functions is generated to interpolate the values of the unknowns within each element. In this case, the base function expresses the pressure field in terms of the characteristics of the medium forming the element. Base functions assume that the unknowns vary in a continuous and smooth way

within the element. Boundary conditions are determined for the system too. These conditions can be either natural, as arising form the balancing between forces in the system, or geometric which are related to the geometric constraints of the problem. Admissible interpolating functions are those which, in this case, are solutions of the wave equation and meet the boundary conditions specified in the problem. The method interpolates the function inside each volume using values of the functions at the vertices that represent the element, also known as nodes. The size of the elements has a direct impact in the accuracy of the interpolations and the final result obtained with this method (Graham 1993).

In the case of Boundary Element Methods (BEM), only the boundaries are discretized using a similar criteria to the one used in the FEM. The boundary conditions are chosen to reflect the characteristics of the enclosed medium. This leads to a lower calculation space but the complexity of the interactions between each discrete volume is higher. FEM is frequently used to calculate the propagation in homogeneous media while BEM is used to calculate the transmitted longitudinal and transverse fields generated beyond interfaces, so a combination of both is suitable to efficiently simulate stationary-wave propagation in complexly shaped, inhomogeneous mediums (Piranda et al. 1998).

General purpose computing on Graphic Processing Units

One of the main problems to be solved when performing simulations of wave propagation is that the computational load of calculating the acoustic fields generated by ultrasound transducers is high because the propagation spaces must be discretized as grids which distance between points depends on the highest frequency used (Piranda et al. 1998).

General purpose computing on Graphic Processing Units (GPGPU) is the term used to categorize simulations and calculations performed in a vari-

ety of fields in science using the parallel processing capabilities of a Graphic Processing Unit (GPU). GPGPU has become popular since the introduction of the Computer Unified Device Architecture (CUDA) programming model (Kirk & Hwu 2010). CUDA allows the user to exploit the parallel processing capabilities of a graphics card to reduce the computing time for problem solving.

Each CUDA-enabled graphics card has a number of streaming multiprocessors (SM), each having a given number of streaming processors (SP). Each SP is multithreaded, which means multiple threads of execution can be launched on each of them at the same time. Threads are organized into blocks and have access to different levels of memory. Adequate utilization of the memory architecture by the program is important to achieve better performance. GPUs have a global memory that can be accessed by all the threads but also provides the slowest bandwidth. Constant memory is similar to global memory and can be accessed by all threads but it is cached, which provides shorter access times when the same portions of memory are accessed continuously. There is a level of shared memory which provides faster access time than the global memory but it is shared only among threads within the same block. Each thread has an individual set of memory locations called registries which provide the lowest latency to memory access but have single thread scope.

Portions of code which are to be executed in a GPU are organized in kernels. When a call to a kernel is performed, the number of blocks and threads to be used by the GPU is specified and all of them will execute the same code. Special care must be taken in the creation of kernels and the specification of the thread organization so that the resources in the GPU are used as efficiently as possible and thus obtaining the best performance possible for a given application.

GPGPU using CUDA has been explored as an alternative to drastically reduce execution times in the simulation of ultrasound acoustic field simulations for visualization, training and treatment planning when compared to applications run on CPUs (Kutter et al. 2009*b*, Reichl et al. 2009). CUDA libraries for the optimized calculation of the Fast Fourier Transform like cuFFT (Corporation n.d.) have been generated and tested, which provides a basis to implement optimized spectral methods in the GPU (Jaros et al. 2012). Algorithms with small amounts of dependencies between calculations from one point to another are highly parallelizable and can also benefit from execution on a graphics card (Hobson et al. 2012).

3.2 Modelling thermally induced bio-effects

3.2.1 Bio heat transfer equation

The bio heat transfer equation (BHTE) is a modification of the basic thermodynamic equation of energy conservation which can be used to calculate thermal effects in tissue. It was first proposed Pennes (1948) and is given by

$$\rho_m C_m \frac{\partial T_m}{\partial t} = K_m \bigtriangledown^2 T_m - w_m C_b (T_b - T_m) + Q_m \tag{3.19}$$

where T_m, ρ_m, K_m, C_m, w_m and Q_m are, respectively, the temperature ($^\circ C$), density (kgm^{-3}), thermal conductivity ($Wm^{-1}\,^\circ C^{-1}$), specific heat ($Jkg^{-1}\,^\circ C^{-1}$), blood perfusion ($mlmin^{-1}100g^{-1}$) and heat generation power density (Wm^{-3}) at point m in the tissue, C_b is the specific heat of blood ($Jkg^{-1}\,^\circ C^{-1}$) and T_b is the arterial blood temperature ($^\circ C$). The equation accounts for the heat conduction of the tissue, the heat transfer from blood perfusion of the tissue and the acoustic energy intake Q_m at the point of interest. The latter term, can be defined as $Q_m = \alpha\beta_{eff}|p_m|^2\rho_t c$, where α is

the acoustic pressure attenuation coefficient, β_{eff} is the coefficient of effective absorption of the tissue and p_m is the pressure amplitude at point m.

Chapter 4

HIU acoustic fields close to bone interfaces

HIU uses acoustic waves propagating into tissue for therapeutic purposes. Energy from the sound waves is absorbed by the tissue and transformed into heat. The way sound propagates in tissue directly impacts the temperature variations in it, and thus the therapeutic outcome. Sound reflects and refracts when crossing an interface between materials with different acoustic properties (ter Haar & Coussios 2007). Tissues are inhomogeneous and often various interfaces appear on the propagation path causing reflexion of the wave, particularly when encountering hard surfaces such as bone. The inhomogeneous nature of most therapeutic target regions for HIU suggests that proper understanding of the acoustic phenomenon involved is attained to ensure safety and efficiency of the procedures. To achieve this purpose, simulations implementing a method which takes into account the forward and reflected waves and their interaction were performed and validated against experimental measurements. Details of the method, implementation of the simulations and validation experiments are subject of the present chapter.

4.1 Materials and methods

4.1.1 Hydrophone measurements of the acoustic field

The first step in this thesis work consisted on generating an experimental observation setup for the phenomenon of sound propagation close to the boundary between a fluid and a solid. For this, a 0.075-mm needle hydrophone (SN:1424, Precision Acoustics, Dorset, UK) was used to measure the pressure amplitude of the acoustic field generated by a 7.29 MHz ultrasound transducer focused at 6 cm and element diameter of 1.27cm (V320-SU-F60MM-PTF, Olympus, Center Valley, PA, USA) (figure 4.1). The hydrophone was placed perpendicular to the wave propagation direction and moved between the transducer and the solid sample (2.5-cm thick transparent acrylic) using a robotic arm to acquire scans (3x3 mm over the xz plane with a step of 0.35λ, where λ is the wavelength) (figure 4.2). The hydrophone was connected to a DC coupler (DCPS006, Precision Acoustics, Dorset, UK) and a booster amplifier (Precision Acoustics, Dorset, UK). The amplified signal was captured by an oscilloscope (WaveRunner 62Xi, LeCroy, New York, USA) and samples were transferred to a PC using Matlab 7.10 (Mathworks, Natick, MA, USA). The experiments were performed inside a tank with degassed water (1 ppm) at 20°C. The center of the acquired scans was set to 4.6 cm and the distance between the transducer and the center of the acrylic was set to 5.6 cm.

To acquire the forward wave, the transducer was excited with 7.29 MHz sinusoidal wave sequences of 30 bursts with a repetition rate of 10 Hz in absence of the acrylic sample. Then, the acrylic sample was placed and the time of flight for the acoustic wave was calculated to ensure that enough bursts were sent to produce an interaction between the forward and reflected waves at the measuring location. Since at least 98 bursts were required to cover the 2 cm distance from the hydrophone to the sample and back with

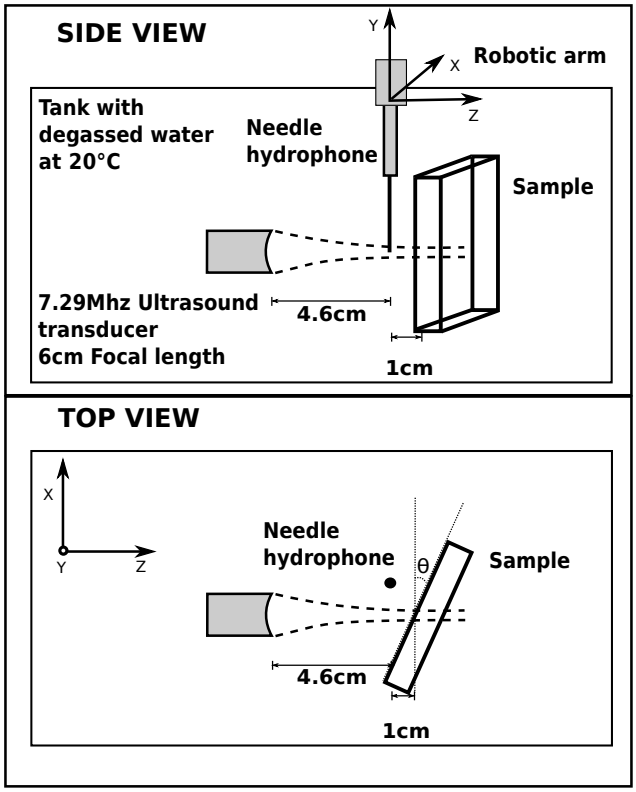

Figure 4.1: Diagram of the first experimental setup where a needle hydrophone is used to characterize the acoustic field produced by a High Intensity Ultrasound transducer facing a solid sample.

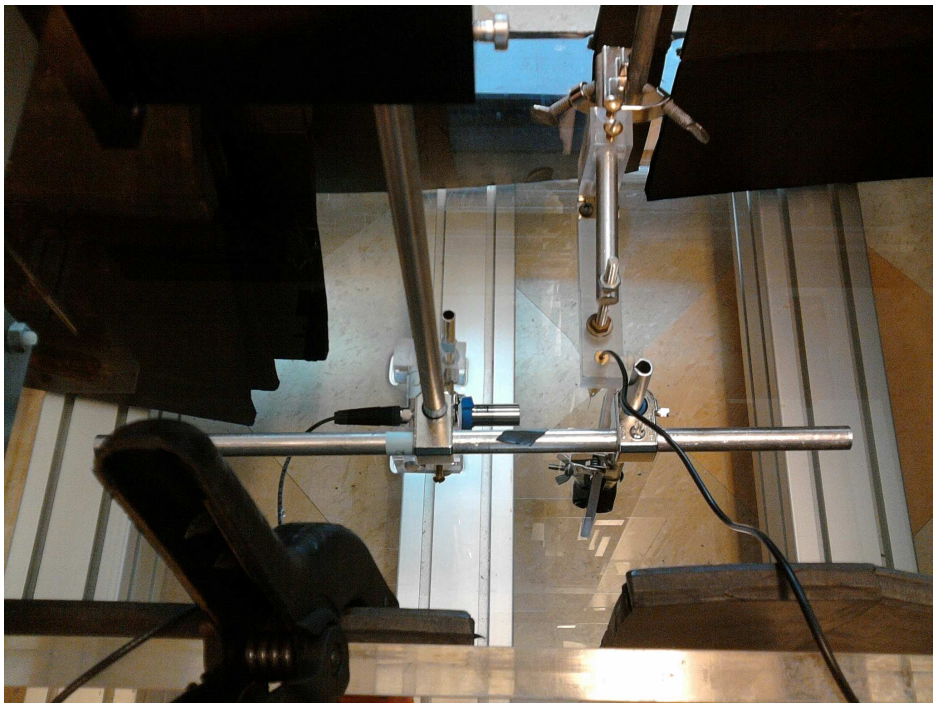

Figure 4.2: Tank, transducer, hydrophone and solid sample submerged in degassed water used in the experimental setup from a top view.

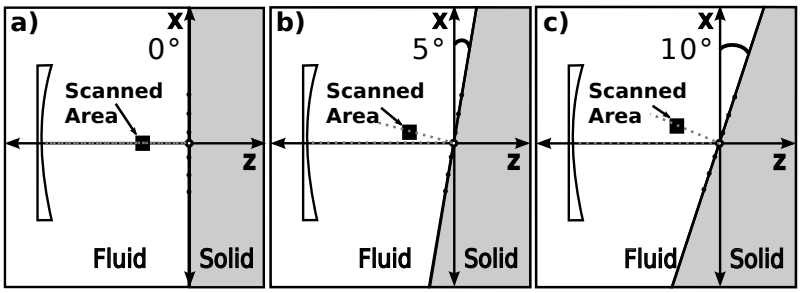

Figure 4.3: Visualization of the acquisition and simulation areas for the hydrophone measurements at an incidence angle of a) 0°, b) 5° and c) 10°.

the selected transducer wavelength, 140 bursts were used in order to provide an interaction window of 5.75μs while avoiding the influence of the reflected wave produced at the other side of the solid sample. The repetition rate was set to 10 Hz to avoid the detection of previous waves still present in the vicinity of the interface.

Scans were acquired at different angles of incidence (0°, 5° and 10°). The center of the solid sample was kept at the same distance from the transducer. The hydrophone was moved in order to keep the center of the scan in line with the center of the forward and reflected wave interaction region (figure 4.3).

4.1.2 Calculation of combined forward and reflected acoustic fields

A plane wave (A) travels through a fluid over the xz plane and a solid surface located at $z = 0$ perpendicular to the wave propagation direction as shown in figure 4.4. At the boundary with the solid surface, three new waves are generated: a reflected longitudinal wave (V) propagating back into the fluid,

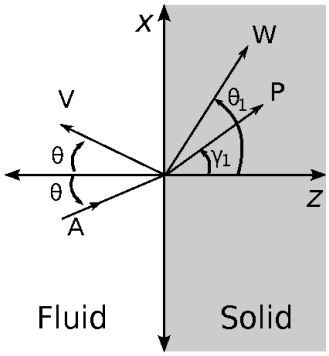

Figure 4.4: Diagram describing the wave propagation scenario at the boundary between a fluid and a solid. θ is the propagation angle of the incident and reflected waves, θ_1 is the propagation angle of the longitudinal transmitted wave and γ_1 is the propagation angle of the transverse transmitted wave

a longitudinal wave (W) and a transversal wave (P) propagating into the solid material (Brekhovskikh & Godin 1998).

To model the interaction between the incident longitudinal wave (A) and the reflected wave (V) generated at the boundary, a modified version of the Rayleigh-Sommerfeld integral was used. This was performed in three stages which are illustrated in figure 4.5.

The first stage (figure 4.5 a) calculates the particle displacement u_f generated by the ultrasound transducer at discrete positions between the transducer and the boundary of the interface by

$$u_f(x,y,z)|_{z<z_b(x,y)} = \frac{1}{2\pi}\sum_n \frac{\exp(ik_0R_n - \alpha R_n)}{R_n} u_{0_n}\delta s_n, \tag{4.1}$$

where k_0 is the wave number, R_n is the distance between the n^{th} element of area δs on the surface of the acoustic source and a point of interest located at coordinates (x,y,z), α is the attenuation coefficient of the fluid, u_{0_n} is the

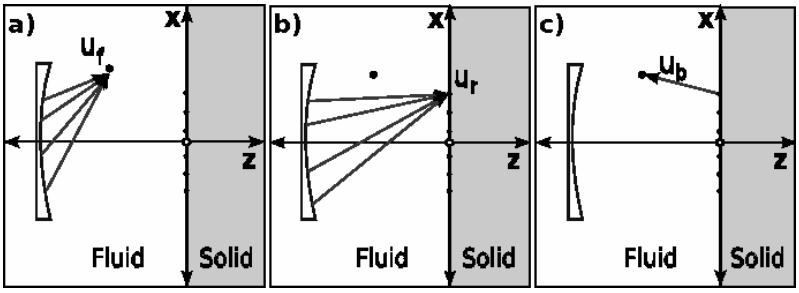

Figure 4.5: Diagram used for Rayleigh-Sommerfeld integral calculations of the forward and reflected waves close to a liquid-solid interface used for a) calculation of the particle displacement induced by the forward wave, b) calculation of the particle displacement at the boundary and c) calculation of the particle displacement induced by the reflected wave.

initial displacement of the n^{th} element on the surface of the acoustic source and $z_b(x, y)$ is the value of the z coordinate at the boundary for given values of x and y. Points located at $z < z_b(x, y)$ belong to the fluid material and points located at $z > z_b(x, y)$ belong to the solid.

The second step (figure 4.5 b) calculates the particle displacement u_r induced by the reflected wave generated at the boundary between both materials and is obtained by

$$u_r(x, y, z)|_{z=z_b(x,y)} = \frac{1}{2\pi} \sum_n V_n \frac{\exp(ik_0 R_n - \alpha R_n)}{R_n} u_{0_n} \delta s_n, \tag{4.2}$$

where V_n is the reflection coefficient at each point on the fluid-solid interface surface. This coefficient depends on the angle of incidence and is obtained by applying boundary conditions for the continuity of the xz tensor, the zz tensor and the particle displacement at the boundary with the solid by the solution of the wave equation (see subsection 4.1.3) and is given

by

$$V_n = \frac{Z_l \cos^2(2\gamma_1) + Z_t \sin^2(2\gamma_1) - Z}{Z_l \cos^2(2\gamma_1) + Z_t \sin^2(2\gamma_1) + Z}, \tag{4.3}$$

where Z is the impedance of the liquid medium, Z_l is the specific longitudinal impedance of the solid medium, Z_t is the specific transversal impedance of the solid medium and γ_1 is the refraction angle of the transverse wave propagating through the solid.

In the third step (figure 4.5 c), the particle displacement u_b generated by the reflecting surface is obtained by

$$u_b(x, y, z)|_{z<z_b(x,y)} = \frac{1}{2\pi} \sum_m \frac{\exp(ik_0 R_m - \alpha R_m)}{R_m} u_{r_m} \delta s_m, \tag{4.4}$$

where the acoustic source now is described by m elements forming the surface of the interface.

Finally, the particle displacement u is obtained by the complex summation of both u_f and u_b

$$u(x, y, z)|_{z<z_b(x,y)} = u_f + u_b \tag{4.5}$$

4.1.3 Derivation of the Reflection Coefficient

The transmission of acoustic waves at liquid-solid boundaries and the derivation of the reflection coefficient at the boundary has been discussed previously in literature (Bruneau & Scelo 2006, Brekhovskikh & Godin 1998, Pierce 1994). Considering a plane wave propagating in a fluid over the xz plane (figure 4.4), the velocity potential of the incident wave can be described by

$$\phi_{inc} = A \exp\left[-ik_0(x \sin(\theta) - z \cos(\theta))\right], \tag{4.6}$$

where k_0 is the wave number, θ is the incidence angle and A is the amplitude of the wave.

At the boundary with a solid surface located at z=0 perpendicular to the direction of wave propagation, a longitudinal wave will be reflected back to the fluid, and two waves (longitudinal and transversal) will be propagated into the solid. The velocity potential of the reflected wave ϕ, the transmitted longitudinal wave ϕ_1 and the transmitted transversal wave Ψ_1 are given by

$$\phi = AV \exp\left[-ik_0(x\sin(\theta) - z\cos(\theta))\right], \tag{4.7}$$

$$\phi_1 = AW \exp\left[-ik_1(x\sin(\theta_1) - z\cos(\theta_1))\right], \tag{4.8}$$

and

$$\Psi_1 = AP \exp\left[-i\chi_1(x\sin(\gamma_1) - z\cos(\gamma_1))\right], \tag{4.9}$$

where V is the reflection coefficient, W is the longitudinal refraction coefficient and P is the shear refraction coefficient, k_1 is the wavenumber of the transmitted longitudinal wave, χ_1 is the wavenumber of the transmitted shear wave, θ_1 is the propagation angle of ϕ_1 and γ_1 is the propagation angle of Ψ_1. The reflection coefficient, which stands for the amount of energy from the forward wave which will be converted into the reflected wave propagating back to the first material, depends on the acoustic properties of both materials.

The total acoustic field in the fluid can be obtained by the sum of transmitted and reflected waves

$$\phi = A[\exp\left[-ik_0(x\sin(\theta) - z\cos(\theta))\right] + Ve^{[-ik_0(x\sin(\theta) - z\cos(\theta))]}]. \tag{4.10}$$

Neglecting the viscosity of the fluid and thus considering the tangential

components of the stresses as zero, W is expressed as

$$W = \frac{-P\chi_1 \cos(2\gamma_1)}{k_1 \sin(2\theta_1)}, \tag{4.11}$$

with P given by

$$P = -\frac{\frac{2\rho_0}{\rho_1} Z_t \sin(2\gamma_1)}{Z_l \cos(2\gamma_1)^2 + Z_t \sin(2\gamma_1)^2 + Z}, \tag{4.12}$$

and V as

$$V = \frac{-Wk_1 \cos(\theta_1)}{k_0 \cos(\theta)} + \frac{P\chi_1 \sin(\gamma_1)}{k_0 \cos(\theta)} + 1, \tag{4.13}$$

where ρ_0 is the density of the fluid and ρ_1 is the density of the solid.

The longitudinal specific impedance Z_l, the transversal specific impedance Z_t and the impedance of the material Z at the boundary are defined as

$$Z = \frac{\rho_0 c}{\cos(\theta)}, \tag{4.14}$$

$$\tag{4.15}$$

$$Z_l = \frac{\rho_1 c_1}{\cos(\theta_1)}, \tag{4.16}$$

$$\tag{4.17}$$

and

$$Z_t = \frac{\rho_1 b_1}{\cos(\gamma_1)}, \tag{4.18}$$

where c is the longitudinal speed of sound in the fluid, c_1 is the longitudingal speed of sound in the solid and b_1 is the shear speed of sound in the solid.

Substituting the values of W and P in 4.13 and using the previous definitions

of Z_l, Z_t and tZ in combination with Snell's law, an expression for V is obtained, given by

$$V = \frac{V_{sup}}{V_+}, \tag{4.19}$$

where V_{sup} is

$$V_{sup} = Z_l \cos(2\gamma_1)^2 + Z_t \sin(2\gamma_1)^2 - Z \tag{4.20}$$

and V_+ is

$$V_+ = Z_l \cos(2\gamma_1)^2 + Z_t \sin(2\gamma_1)^2 + Z. \tag{4.21}$$

Finally, the reflection coefficient V can be expressed as

$$V = \frac{Z_l \cos^2(2\gamma_1) + Z_t \sin^2(2\gamma_1) - Z}{Z_l \cos^2(2\gamma_1) + Z_t \sin^2(2\gamma_1) + Z}. \tag{4.22}$$

4.1.4 Implementation

The proposed model was implemented using Matlab 7.10 (MathWorks, Natick, Massachusetts, USA) in combination with MEX Files coded in CUDA to take advantage of the parallel processing capabilities of the GPU. Figure 4.6 shows a block diagram of the simulation.

The calculation space consists of a 3D grid which defines the points that form the propagation media and grid which defines the points located at the boundary between the fluid and the solid material. The algorithm also uses a 3D matrix which defines the points which form the acoustic source.

In the first step of the calculations, the propagation media data structure is sent to the MEX function and stored in global memory. The matrix for the acoustic source points is also sent as input but stored in constant memory of

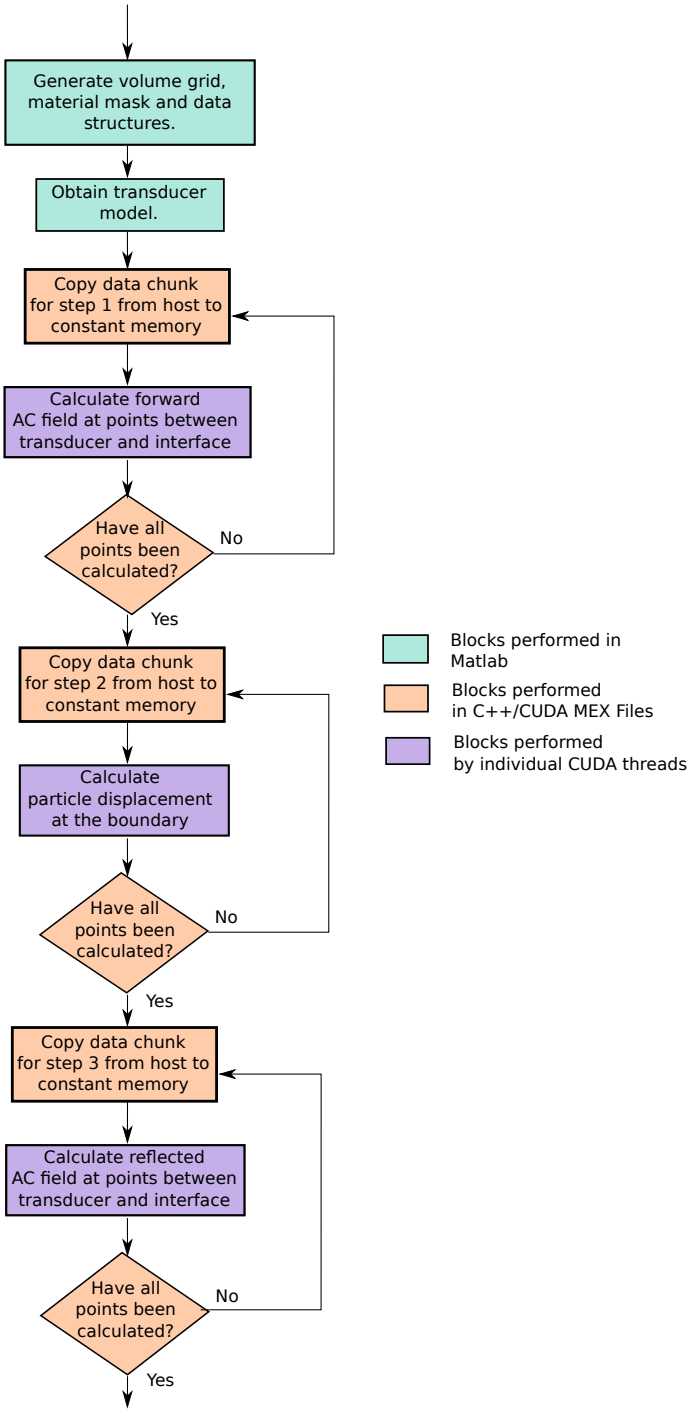

Figure 4.6: Diagram of the steps taken to calculate the acoustic field at each point between the transducer and the fluid-solid interface.

the GPU as well as the attenuation, speed of sound, density and wave number. The acoustic source points matrix is a large structure, thus it has to be partitioned in several chunks and copied part by part to constant memory. The kernel is called several times until all the source points have been considered in the kernel. The pseudocode of the C call to the kernel is as follows:

```
set mr1start to 0;
set LastPart to 0;
set mr1end to 0;

set thread block size to CUDA_THREADBLOCKLENGTH in x and 1 in y

set nBlockSizeX to (target_point_size-1)/dimThreadBlock.x + 1;
set nBlockSizeY to 1;

if nBlockSizeX more than 65534
  assign (nBlockSizeX/65534) to nBlockSizeY;
  if nBlockSizeX %65534  not equal to 0
    increment nBlockSizeY
  assign nBlockSizeX/nBlockSizeY+1 to nBlockSizeX;
end if

set block dimensions to nBlockSizeX and nBlockSizeY;

// Run the kernel several times until all data chunks have been processed
while mr1start is less than size_of_source_points

  set mr1stop to mr1start + chunk_size;
  if (mr1stop more than or equal to size_of_source_points)
      set mr1stop to size_of_source_points;
      indicate that this is the last chunk;
```

```
  end if

  assign mr1stop - mr1start to mr1step;

  copy source_points chunk from host to constant memory;
  copy initial_particle_displacement chunk from host to constant memory;

  call ForwardPropagationKernel;

  check for errors;
  sincronize threads;
  increment mr1start by mr1step;
end while;
```

One thread is assigned to each point in the propagation media structure for which the particle displacement needs to be calculated. To achieve this, a 2D block grid is generated by dividing the total amount of points available by the maximum block size in x times the number of threads per block which was defined to 512. Single precision operations are used to calculate the complex pressure field which, as seen in section 4.1.2 is actually a summation of contributions from each source point. Partial results of the summation are stored in a registry to enhance performance and then copied to global memory when all the provided source points have been accounted for. The pseudocode for this kernel is shown below.

```
ForwardPropagationKernel
  set thread_id to (blockIdx.y*gridDim.x + blockIdx.x)
    *blockDim.x + threadIdx.x;
  declare temp_r and temp_i;

  if thread_id less than size_of_target_points
```

```
    set temp_r and temp_i to 0;
    while si1 is lower than size_of_source_points loop
      calculate the distance from source_point[si1] to target_point[thread_id]
      assign __expf(R*wvnbi)*Part_a1pr[si1]/R to ti;
      assign ti to tr;
      calculate the sin and cos of R*wvnbr and assign them to pSin and pCos;
      multiply tr by (initial_real_particle_displacement[si1]*pCos
      + initial_imaginary_particle_displacement[si1]*pSin);
      multiply ti by (initial_real_particle_displacement[si1]*pCos
      -initial_imaginary_particle_displacement[si1]*pSin);
      increment temp_r by tr;
      increment temp_i by ti;
      increment si1 by 1;
    end while

    increment u2pr[thread_id] by temp_r;
    increment u2pi[thread_id] by temp_i;

    if this is the last chunk
      assign u2pr[thread_id] to temp_r;
      assign u2pi[thread_id] to temp_i;
      assign  temp_r to R;
      assign -temp_r*wvnbi-temp_i*wvnbr to temp_r;
      assign R*wvnbr-temp_i*wvnbi to temp_i;
      assign temp_r/(2*pi) to u2pr[thread_id];
      assign temp_i/(2*pi) to u2pi[thread_id];
    end if;
  end if;
end ForwardPropagationKernel
```

Table 4.1 shows values for this kernel (ForwardPropagationKernel) obtained by the CUDA GPU occupancy calculator. The hardware version functions $\_\_sinf(x)$, $\_\_cosf(x)$ and $\_\_expf(x)$ were used in the code without

significant loss of accuracy. The final summation is sent back to Matlab as result of the first step.

Table 4.1: Values obtained with the CUDA GPU occupancy calculator for acoustic field calculation Kernel 1 and 2, considering compute capability of 3.0.

Occupancy Calculator Variable	Kernel 1	Kernel 2
Threads Per Block	512	512
Registers Per Thread	26	17
Shared Memory per Block	61 bytes	121
Active Threads Per Multiprocessor	2048	2048
Active Wraps Per Multiprocessor	64	64
Active Thread Blocks Per Multiprocessor	4	4
Occupancy Of Each Multiprocessor	100%	100%

In the second step, the particle displacement at the boundary is calculated. For this, the structure containing the points at the boundary is sent as input to a second MEX function and stored in global memory of the GPU.

The acoustic source data structure is also provided as input and again copied to constant memory in chunks along with the density and speed of sound of both materials in the interface in order to calculate the acoustic impedance.

Both kernels make use of memory coalescing as the memory is accessed in a sequential way by neighboring threads. This allows better access times to global memory. No shared memory is used, as the elements in global memory are read and used only once. The angle of incidence between each point of the source and each point at the boundary is calculated and used to obtain the reflection coefficient. Partial results of the summations are also stored in registries to enhance the performance. Regarding GPU resource usage, table 4.1 shows values for this kernel (ForwardPropagationWindowKernel) obtained by the CUDA GPU occupancy calculator. The pseudocode of the second CUDA kernel is as follows:

```
ForwardPropagationWindowKernel
  set thread_id to (blockIdx.y*gridDim.x + blockIdx.x)
    *blockDim.x + threadIdx.x ;
  declare temp_c, temp_l and temp_s;
  if  thread_id is less than target_points_size
    set temp_c, temp_l and temp_s variables to 0;
    set si1 to 0;
    while si1 is less than size_of_source_points loop
      calculate distance from source_point[si1]
 to target_point[thread_id];
      calculate angle_of_incidence using the distance;

      Calculate reflection coefficient using the angle_of_incidence;
      Calculate transmitted_longitudinal coefficient;
      Calculate transmitted_shear coefficient;
      multiply the reflection coefficient by the initial displacement
and store the result in temp_c;
      multiply the transmitted_longitudinal coefficient by the initial
displacement and store the result in temp_l;
      multiply the transmitted_shear coefficient by the initial
displacement and store the result in temp_s;
    end while

    increment u2Reflected_r[thread_id] by temp_c.re;
    increment u2Reflected_i[thread_id] by temp_c.im;
    increment u2TransLong_r[thread_id] by temp_l.re;
    increment u2TransLong_i[thread_id] by temp_l.im;
    increment u2TransShear_r[thread_id] by temp_s.re;
    increment u2TransShear_i[thread_id2] by temp_s.im;

    if this is the last chunk
```

```
      //Reflected
      assign -i*wvnb*u2Reflected_r[thread_id]*/(2*pi)
     to u2Reflected_r[thread_id];
      assign -i*wvnb*u2Reflected_i[thread_id]*/(2*pi)
     to u2Reflected_i[thread_id2];
      //Long
      assign -i*wvnb*u2TransLong_r[thread_id*/(2*pi)
     to u2TransLong_r[thread_id];
      assign -i*wvnb*u2TransLong_i[thread_id]*/(2*pi)
     to u2TransLong_i[thread_id];
      //Shear
      assign -i*wvnb*u2TransShear_r[thread_id]*/(2*pi)
     to u2TransShear_r[thread_id];
      assign -i*wvnb*u2TransShear_i[thread_id2]*/(2*pi)
     to u2TransShear_i[thread_id];

    end if
  end if
end ForwardPropagationWindowKernel
```

The results of the calculations performed in the second stage are sent back to Matlab.

In the final stage the grid containing the points at the boundary is used as acoustic source and the particle displacement is calculated at the points forming the grid of the propagation media using the same MEX file and kernel described for the first step. The result is added to the particle displacement obtained in the first step by performing a complex summation of both.

4.1.5 Simulation

The acoustic field generated by a circular transducer with the same characteristics as the one used in the experimental setup was calculated within a rectangular volume (40 mm on x, 10 mm on y and 56 mm along z). The spacing between points in the simulated grid as well as between the particles forming the boundary was set to 0.35λ. Table 4.2 shows values for the acoustic properties used to model each material. The liquid was modeled as water and the solid as transparent acrylic. Simulations were performed where the boundary was rotated 0°, 5° and 10° with respect to the x axis.

Table 4.2: Acoustic properties of materials used in the experimental setups and simulations.

Material	Longitudinal speed of sound (m/s)	Transversal speed of sound (m/s)	Attenuation (db/cm/MHz)	Density (g/L)
Water	1480[c]	-	0.002[c]	1000[c]
Transparent Acrylic	2750[a]	1430[e]	1.28[a]	1190[a]
Zedine® Ployacrylaminade	1540[b]	-	0.5[b]	1030[b]
ABS (bone mimic)	2496[d]	1458[d]	11.2[d]	968[d]
Soft tissue	1500[f]	-	0.5[f]	1000[f]
Cortical Bone	2333[f]	1800[f]	21.71[f]	1700[f]

[a] (Selfridge 1985)
[b] (NDjin et al. 2012)
[c] (Azhari 2010)
[d] Provided by Ritesh Patel (Sunnybrook Health Sciences Centre, Toronto, ON, Canada)
[e] (Hydro 2013)
[f] (Burtnyk 2011)

Table 4.3: Average absolute error, pressure increments and peak pressure increments between experimental measurements and simulations.

Incidence angle	Average absolute error	Average pressure increment	Peak pressure increment
0° both waves	3.90% ± 0.54%	10.4%	25.4%
5° both waves	8.18% ± 0.79%	41.63%	130.9%
10° both waves	7.23% ± 0.47%	64.14%	267.18%
0° only forward	26.08% ± 0.84%	N/A	N/A
5° only forward	28.24% ± 1.24%	N/A	N/A
10° only forward	18.52% ± 1.36%	N/A	N/A

4.2 Results

4.2.1 Simulation performance

Simulations were run on an Intel Xeon CPU at 2.13 Ghz with 12Gb in RAM and a Tesla K20 GPU (NVIDIA, Santa Clara, CA, USA). Calculation of a 845x845 plane with CUDA takes 1.36 s. Simulations were also run on a Tesla C1060 GPU. Execution time using it was 5.7170 s. Previous implementation using Message Passing Interface (MPI) took 71.2 s on a 15 machine cluster of Quad-core Intel Xeon CPUs at 2.33GHz.

4.2.2 Validation with hydrophone measurements

The experimental and simulated normalized pressure amplitude for an incident angle of 0°, 5° and 10° are shown in figure 4.7, 4.8 and 4.9 respectively. There was a good agreement between experimentation and simulation when considering the forward, reflected and the combination of the waves. The interference patterns between the forward and reflected waves can be clearly depicted both in the experimental measurements and simulations.

Comparisons of the average absolute normalized difference in the pressure amplitude between the measurements and the simulations were performed

considering both the forward and the reflected wave. Error calculations were also made between the experimental measurements and the simulation with only the forward wave in order to evaluate the impact of not taking into account the reflected wave in the simulations. The results are shown in table 4.3.

The reflected wave causes, as expected, an increase in pressure given by constructive interference of waves and the pressure increases as much as 64.14% average for some cases and up to 267.18% peak (see table 4.3).

As it can be observed, the discrepancy between the simulation and experimental measurements is higher when the reflection is not taken into account with more than 20% additional error for some cases.

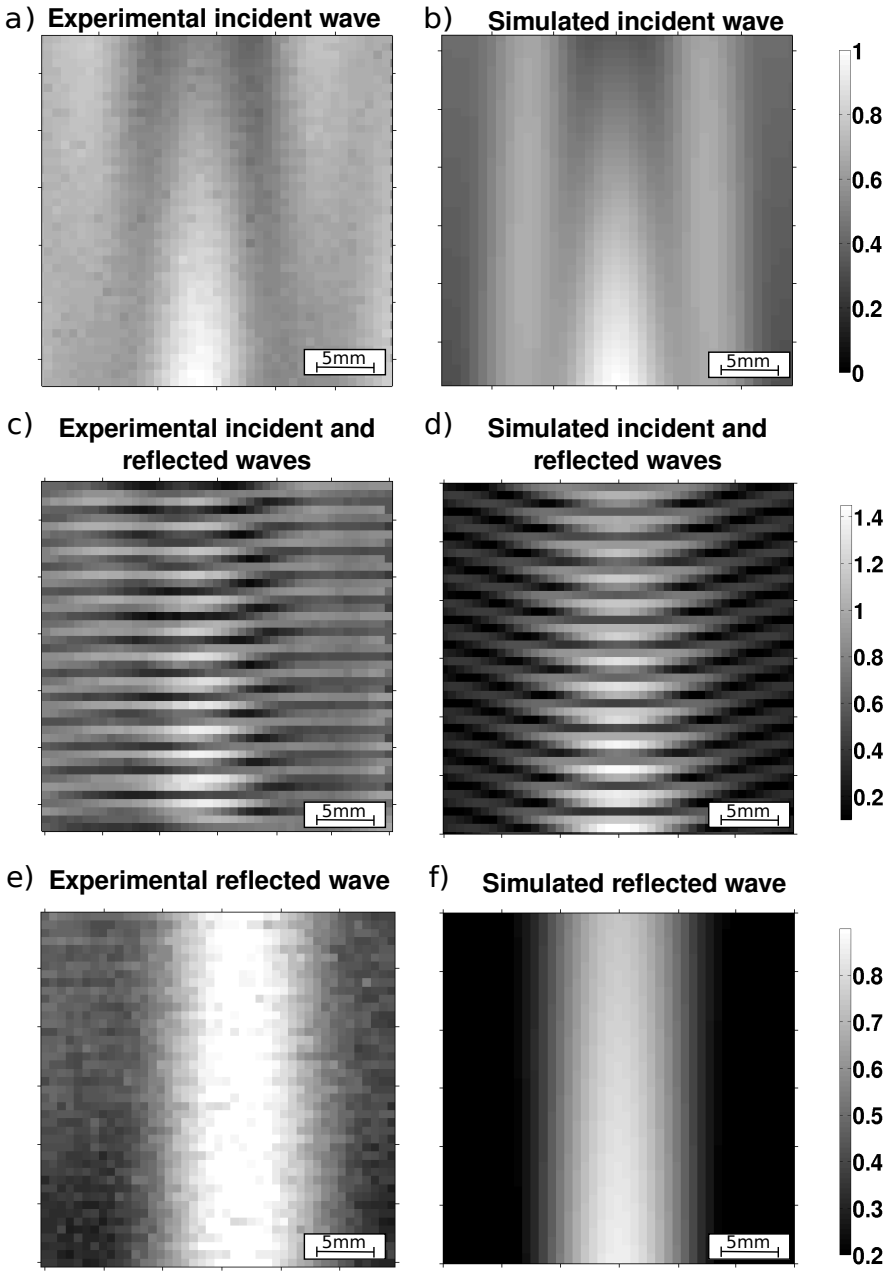

Figure 4.7: Experimental (left) and simulated (right) pressure amplitude (normalized against max value of forward wave measurements) obtained with the liquid-solid interface at 0° with respect to the x axis when forward (a,b), reflected (c,d) and both (e,f) waves are present. Images are centered at 0 mm on the horizontal x axis and 46 mm on the vertical z axis.

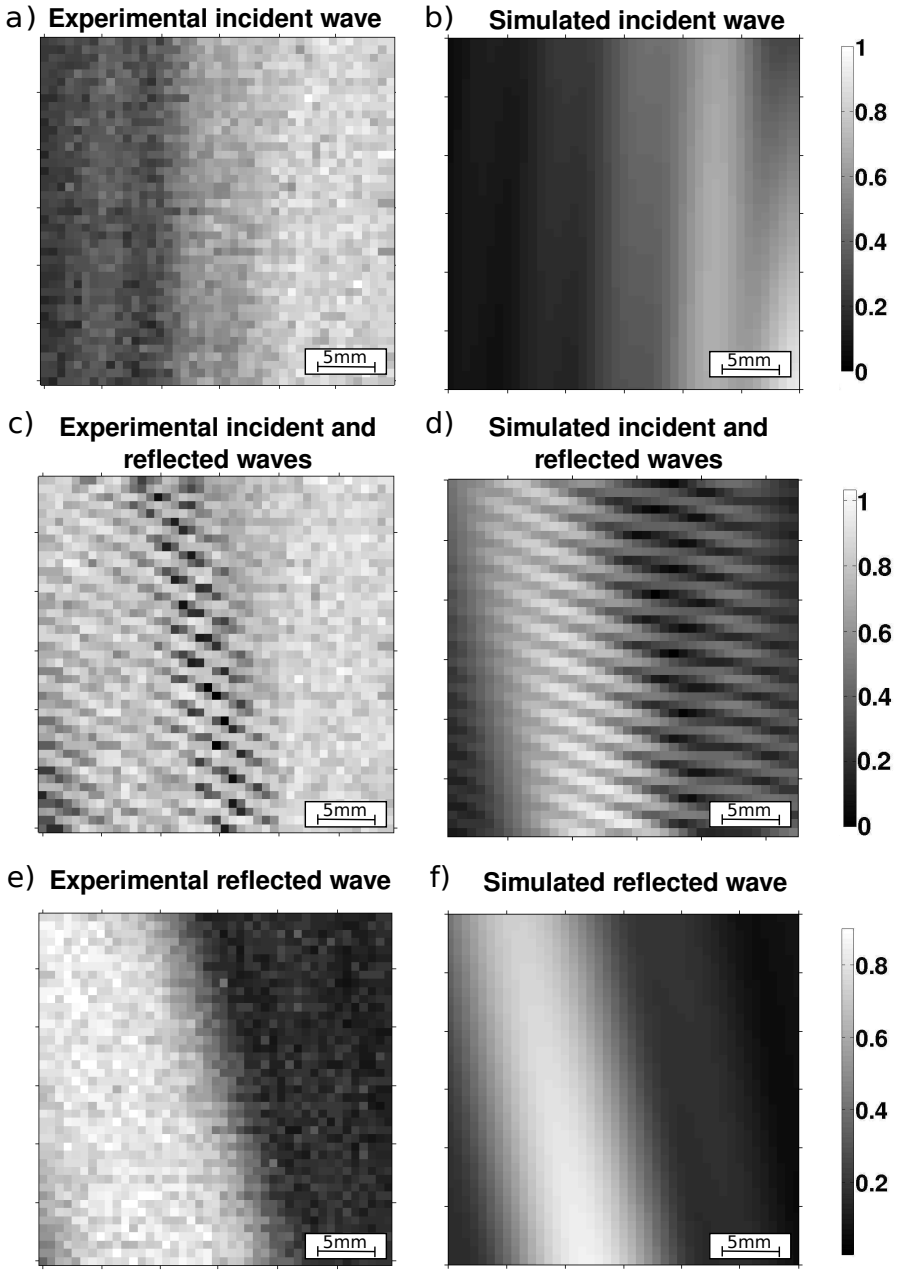

Figure 4.8: Experimental (left) and simulated (right) pressure amplitude (normalized against max value of forward wave measurements) obtained with the liquid-solid interface at 5° with respect to the x axis when forward (a,b), reflected (c,d) and both (e,f) waves are present. Images are centered at -1.5 mm on the horizontal x axis and 46 mm on the vertical z axis.

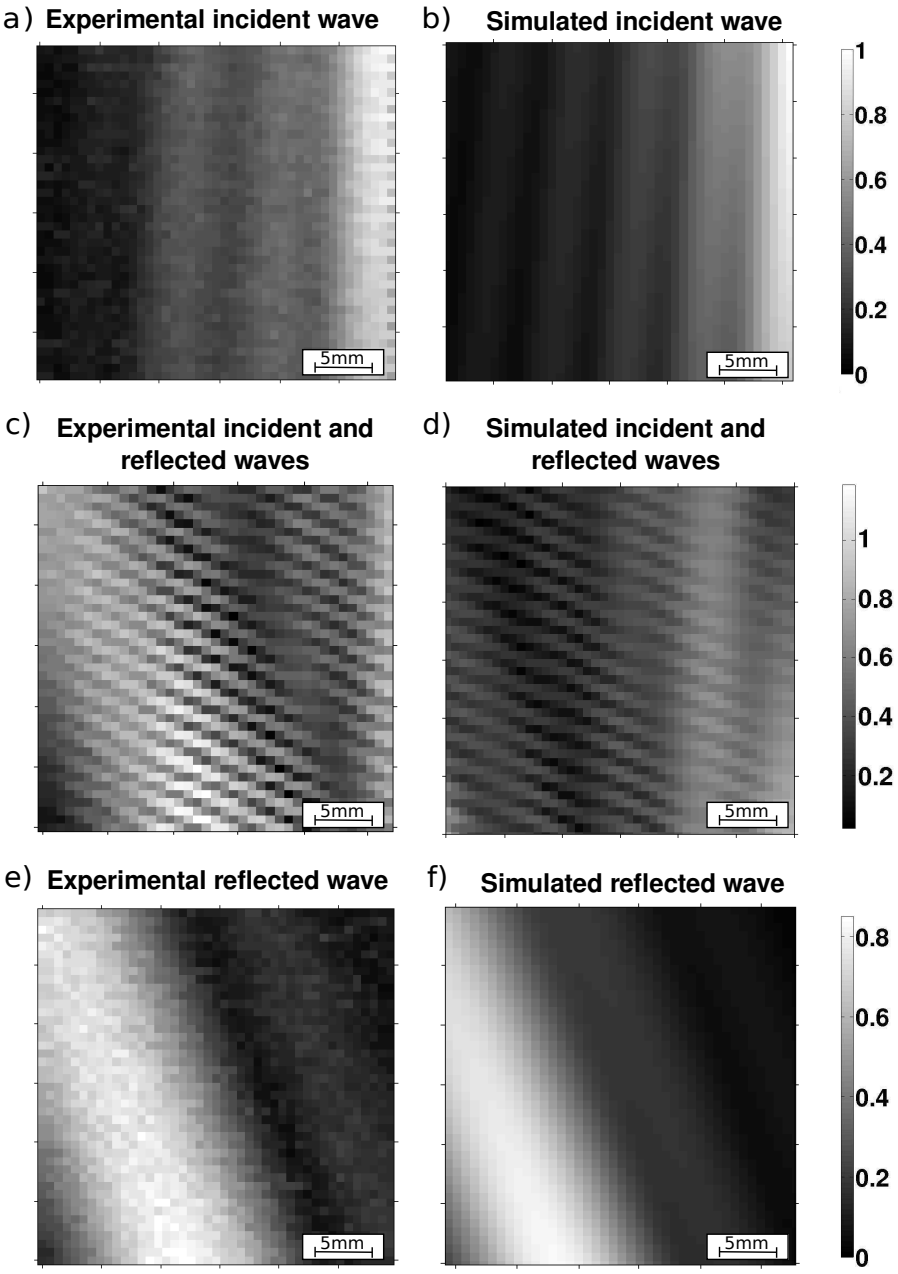

Figure 4.9: Experimental (left) and simulated (right) pressure amplitude (normalized against max value of forward wave measurements) obtained with the liquid-solid interface at 10° with respect to the x axis when forward (a,b), reflected (c,d) and both (e,f) waves are present. Images are centered at -3 mm on the horizontal x axis and 46 mm on the vertical z axis.

Chapter 5

Thermal bio-effects induced by HIU close to bone interfaces

5.1 Materials and methods

5.1.1 Experimental measurements using MRI-based thermometry

The experimental setup was designed to emulate a scenario where the sacrum bone is found at different distances from a trans-urethral HIU device. A phantom with an spiral shape with a planar transducer located at its center was chosen in order to simulate diverse distances between the transducer and the pelvic bone (figure 5.1).

The transducer had three 4x5-mm active elements working at 4.58 MHz. Each element generated an ultrasound wave with a variable effective acoustic power between 0 and 4 W while the device rotated at 0.3°/s around the y axis. The phantom was made of Zedine® (Computerized Imaging Reference Systems,Inc., Norfolk, VA, US) polyacrylaminade gel material surrounded by acrylonitrile butadiene styrene (ABS). The initial radius of the spiral-shaped

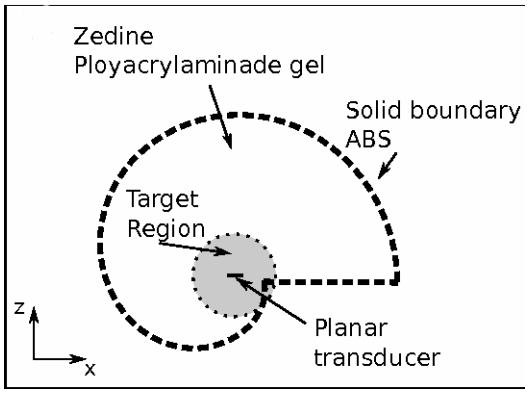

Figure 5.1: Spiral-shaped layered phantom experimental diagram

base of the phantom was 17.5 mm and the final radius was 50.5 mm. Thermal maps were calculated using a proton resonant shift technique (Rieke & Pauly 2008) on a Philips Achieva 3T MRI scanner with a T1-based thermometry sequence (TE = 15 ms, TR = 90 ms, FOV= 160x160x25 mm, Slice thickness = 5 mm, 5x1x1 mm voxel, 5.1 s frame rate, α = -0.0095 ppm/°C and baseline temperature = 22°C). A circular target area of 20 mm in radius was defined around the transducer. The goal was to reach a temperature of 40°C at the boundary of the target region (Chopra et al. 2008).

5.1.2 Calculation of the thermal bio-effects

The algorithm for the calculation of the thermal bio-effects implements the steady-state solution of Eq. 3.19 with a finite difference time differences approach similar to the one described in (Yin et al. 2006). The numerical implementation is

$$T_{i,j,k}^{n+1} = T_{i,j,k}^{n} + \frac{\Delta t}{\rho_{t_{i,j,k}} C_{t_{i,j,k}}} \cdot \{K_{ti,j,k}[P(T_{i,j,k}^{n}, x_i) + Q(T_{i,j,k}^{n}, y_j) + R(T_{i,j,k}^{n}, z_k)] - \omega_{i,j,k} C_{b_{i,j,k}}[T_{i,j,k}^{n} - T_a] + \frac{x_{i,j,k}|p_{i,j,k}|^2}{\rho_{ti,j,k} C_{bi,j,k}}\} \quad (5.1)$$

where $T_{i,j,k}^{n+1}$ is the temperature in the current time step $n+1$ at point i, j, k, $T_{i,j,k}^{n}$ is the temperature in the previous time step n, $C_{t_{i,j,k}}$ is the specific heat, $C_{b_{i,j,k}}$ is the specific heat of blood, $\omega_{i,j,k}$ is the blood perfusion, and

$$P(T_{i,j,k}^{n}, x_i) = \frac{\frac{T_{i-1,j,k}^{n} - T_{i,j,k}^{n}}{x_{i-1}^{n} - x_i^{n}} - \frac{T_{i,j,k}^{n} - T_{i+1,j,k}^{n}}{x_i^{n} - x_{i+1}^{n}}}{\frac{x_{i-1}^{n} - x_i^{n}}{2} - \frac{x_i^{n} + x_{i+1}^{n}}{2}}, \quad (5.2)$$

$$Q(T_{i,j,k}^{n}, y_j) = \frac{\frac{T_{i,j-1,k}^{n} - T_{i,j,k}^{n}}{y_{j-1}^{n} - y_j^{n}} - \frac{T_{i,j,k}^{n} - T_{i,j+1,k}^{n}}{y_j^{n} - y_{j+1}^{n}}}{\frac{y_{j-1}^{n} - y_j^{n}}{2} - \frac{y_j^{n} + y_{j+1}^{n}}{2}}, \quad (5.3)$$

and

$$R(T_{i,j,k}^{n}, z_k) = \frac{\frac{T_{i,j,k-1}^{n} - T_{i,j,k}^{n}}{z_{k-1}^{n} - z_k^{n}} - \frac{T_{i,j,k}^{n} - T_{i,j,k+1}^{n}}{z_k^{n} - z_{k+1}^{n}}}{\frac{z_{k-1}^{n} - z_k^{n}}{2} - \frac{z_k^{n} + z_{k+1}^{n}}{2}}. \quad (5.4)$$

The algorithm was implemented in a MEX file written in C++ and CUDA which is called from a Matlab function. The structure of the implementation is based on the work by Hobson et al. (2012).

To define the acoustic and thermal characteristics of the propagating medium, matrices of properties were created to identify each type of tissue simulated. In this case only water, muscle and bone were defined. A mask was created in Matlab defining which grid points correspond to each type of tissue and their corresponding perfusion rate, thermal conductivity, specific heat, acoustic absorption and density. The grid generated as well as

the matrices containing the acoustic and thermal values were passed to the MEX file as input and stored in global memory. Time exposure and the time step were also sent to the Mex File and stored in constant memory. Kernel calls for the calculation of the temperature at each time step are performed successively to meet the stability conditions of the Finite Differences Time Domain technique until the exposure time was reached.

The temperature at each point was calculated by a CUDA thread. Thermal and acoustic values were copied to shared memory to increase the performance of the execution. Temporal and spatial dependencies are observed in the algorithm as the temperature at each point depends on the temperature in the previous step of the neighboring points in the three cartesian axis. A padding technique was implemented to overlap the calculations and obtain accurate results at the boundaries between blocks.

Table 5.1: Values obtained with the CUDA GPU occupancy calculator for BHTE Kernel, considering compute capability of 3.0.

Occupancy Calculator Variable	BHTE Kernel
Threads Per Block	512
Registers Per Thread	32
Shared Memory per Block	4708 bytes
Active Threads Per Multiprocessor	2048
Active Wraps Per Multiprocessor	64
Active Thread Blocks Per Multiprocessor	4
Occupancy Of Each Multiprocessor	100%

Table 5.1 shows values for this kernel obtained by the CUDA GPU occupancy calculator. The hardware version functions $\_\_sinf(x)$, $\_\_cosf(x)$ and $\_\_expf(x)$ were used in the code without significant loss of accuracy.

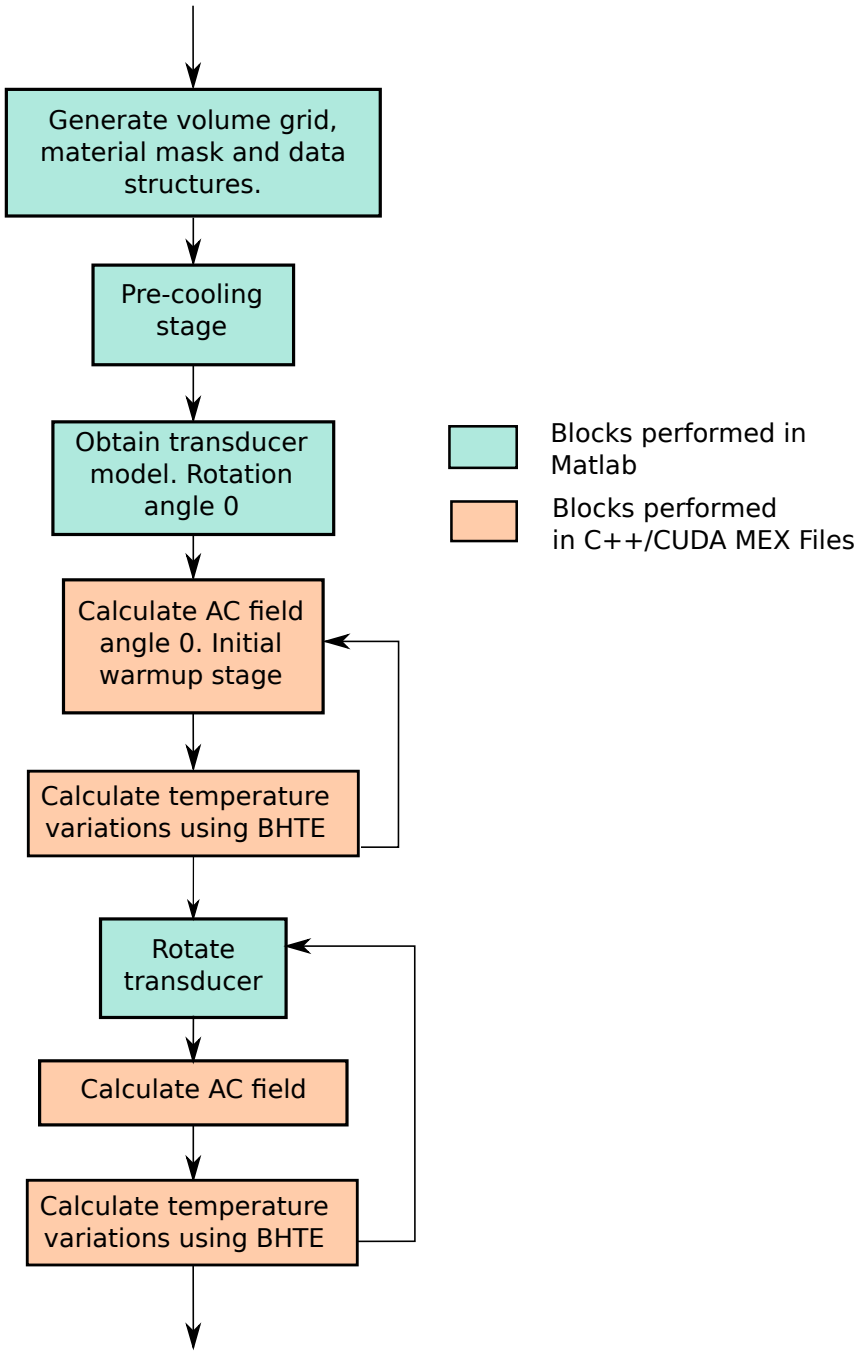

Figure 5.2: Diagram of the steps taken to simulate the proposed method.

Table 5.2: Properties of materials used in the experimental setups and simulations.

Material	Specific heat capacity (J/kg/°C)	Thermal conductivity (W/m/°K)	Absorption Coefficient
Zedine® Ployacrylaminade	3810[a]	0.39[a]	0.7[b]
ABS (bone mimic)	1800[c]	0.25[c]	0.9[d]
Soft tissue	3700[b]	0.5[b]	0.6-0.97[b]
Cortical bone	1600[b]	0.6[b]	0.9[d]

[a] (NDjin et al. 2012)
[b] (Burtnyk 2011)
[c] Provided by Ritesh Patel (Sunnybrook Health Sciences Centre, Toronto, ON, Canada)
[d] Estimated

5.1.3 Simulation

For the simulations, a spiral-shaped grid with an initial radius of 17.5 mm and a final radius of 50.5 mm on the xz plane was extruded 15mm over the y axis. The spiral-shaped volume was enclosed in a box of dimensions 51mm on x, 51 mm on z and 15 mm on y. The points in the grid were separated 0.5λ from each other.

The volume inside the spiral was modelled as Zerdine® polyacrylaminade gel and the volume between the spiral and the enclosing box as ABS (bone mimic). The thermal characteristics of each material can be seen in table 5.2.

The transducer was modelled as a planar array with the same characteristics as described for the experimental setup. Each element was discretized as an array of smaller elements of area $ds = (0.5\lambda)^2$. The simulation was time-dependent and a temperature map was generated by calculating the acoustic field for different positions of the transducer as it was rotated over

the y axis and then giving this as input for an algorithm implementing the BHTE. Figure 5.2 shows a block diagram of the simulation.

The initial conditions of the simulation were generated by performing a precooling stage in which water at 17.5°C was considered to be running at a speed of 1 L/min through a tube of 4.2 mm in diameter within which the transducer was located. A preliminary simulation was executed until reaching a steady state where the maximum temperature change within a period of 5 seconds was less than 0.01°C. This initial simulation ensured that the modelling conditions matched as close as possible the experiments.

After this initial condition was achieved, an initial warm up stage was performed in which the transducer was modelled and set at an angle of 0° over the y axis. The acoustic field was calculated as detailed in 4.1.4 using the same power parameters used during the experimental measurements. Simulations using the BHTE algorithm described section 5.1.2 were performed using the calculated acoustic field as input. Temporal derivatives were computed with a forward differencing scheme and the time step was chosen to be 0.01 s for 4.7 Mhz accordingly to the grid spacing used. The transducer was not rotated until a steady temperature at the limit of the target region of 40°C was obtained. Then, successive rotations in steps of 1.5° over the y axis were performed, following the same rotational speed used for the experimental measurements. At each rotation position, the acoustic pressure field was calculated and then used as input for the BHTE algorithm for a simulated exposition time of 5 seconds.

5.2 Results

5.2.1 Simulation performance

Simulations were run on an Intel Xeon CPU at 2.13 Ghz with 12Gb in RAM and a Tesla K20 GPU (NVIDIA, Santa Clara, CA, USA). The precooling stage considering a volume of 971×971×18 points took 98496 s (1.14 days). This stage has to be performed only once. Calculation of the acoustic field for each time step takes 6.2s. Calculation of the BHTE thermal map within the same volume for each time step took 420 s. The whole simulation, consisting on 182 steps, took 108864 s (1.26 days) to run.

Simulations using a Tesla C1060 GPU were also performed. Calculation of the acoustic field for each time step take 31.7s. Calculation of the BHTE thermal map within the same volume takes 1749.6 s. The whole simulation took 481248 s (5.57 days) to run.

5.2.2 Validation with MRI-based thermometry

The results of the simulation and the experimental data at different time points (380, 550, 650 and 730 seconds) during the HIU exposure can be seen in figure 5.3. Three-hundred and eighty seconds after the heating started, an increment in temperature in the region close to the boundary between materials starts to be visible in the experimental data but it can not be detected yet in the simulation. After 650 seconds, the region presenting an increment in temperature can be observed in both the experimental data and the simulation considering the reflected wave, although it can not be observed if the reflected wave is not taken into account (right column). The non targeted heating area reaches temperatures above 40°C.

A comparison between measured and simulated temperature averaged

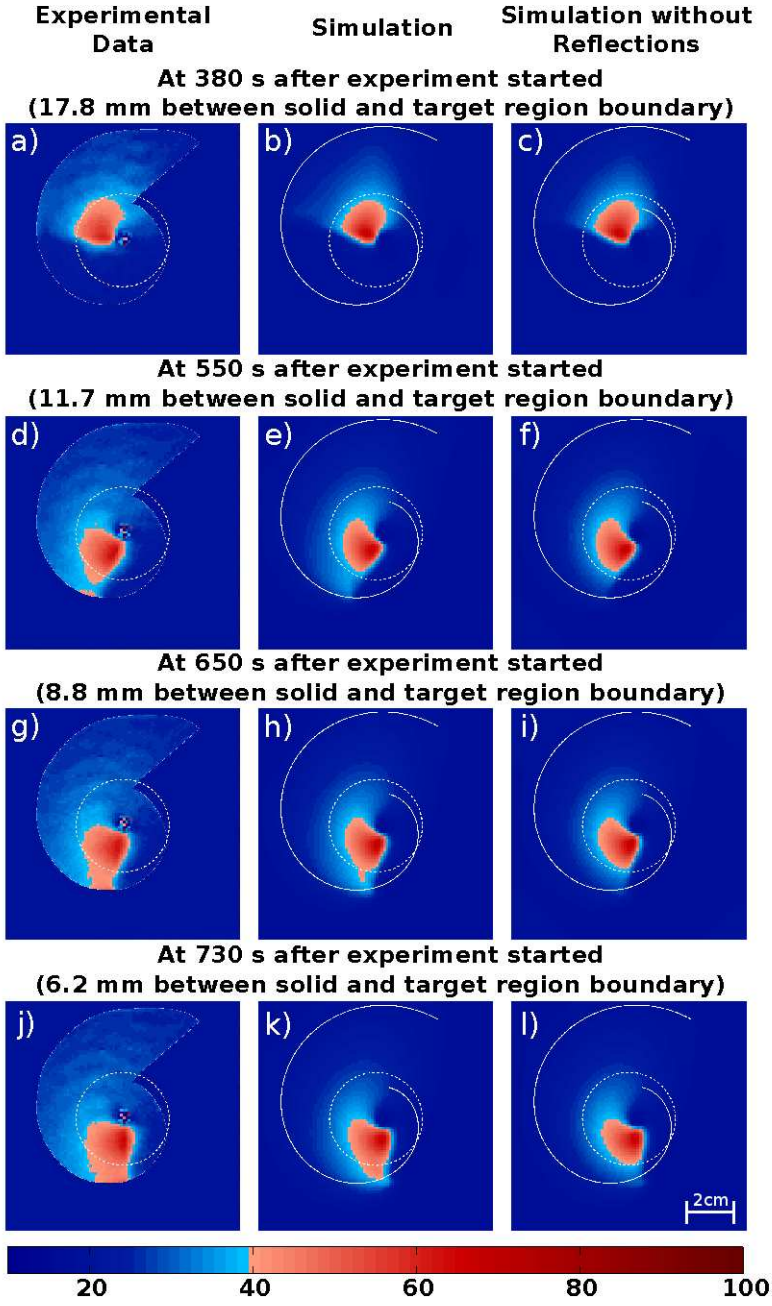

Figure 5.3: Experimental (left) and simulated thermometry results considering the reflected wave (centre) and without the reflected wave (right) calculated 380 s (a,b,c), 550 s (d, e, f), 650 s(g, h, i) and 730 s (j, k, l) after the start of heating. Image scale is 10 cm in both directions (z and x). The color scale was chosen to show clearly the over heating above 40° C

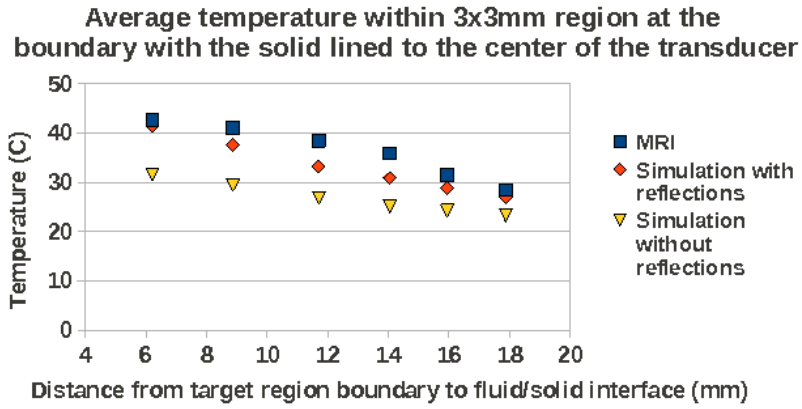

Figure 5.4: Average temperature measured within a 3×3×5-mm region at the boundary between the fluid and the solid.

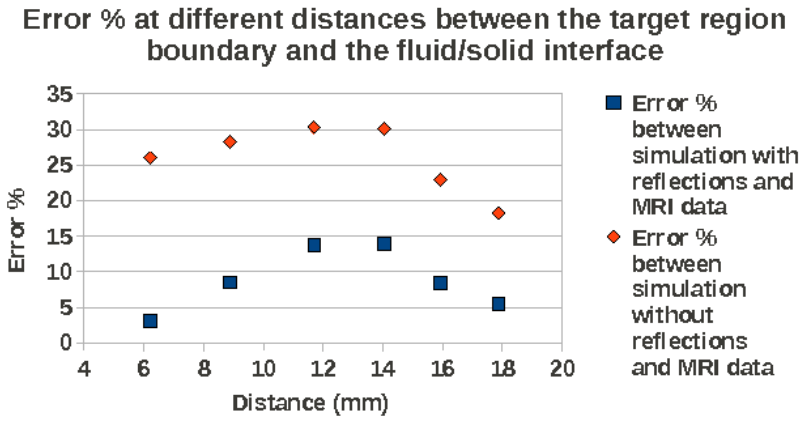

Figure 5.5: Error within a 3×3×5-mm region at the boundary between the fluid and the solid.

within a 3×3×5 mm volume located at the boundary for different positions of the transducer is shown in figure 5.4. Figure 5.5 shows the error values corresponding to figure 5.4. The regions of interest were chosen to be in line with a parallel line drawn from the center of the face of the transducer at each rotation position. The error obtained when the reflected wave is neglected is consistently higher that the one observed for the simulations considering the reflections. This becomes more significant as the distance between the boundary and the transducer becomes smaller because higher increments of temperature are disregarded. The error in the calculated temperatures can be as high as 30% when the reflected wave is not taken into account. The error reaches a maximum value at specific positions of the transducer (12 to 14 mm between the boundary of the target region and the solid interface).

Chapter 6

Discussion and Conclusions

This work shows a simple method to accurately predict temperature and pressure generated by a HIU transducer at solid boundaries. The main advantage and originality of the method is the possibility to obtain fast and simple implementations that could allow for cost-efficient simulations that can be easily used during planning and for transducer design. This method is particularly useful for accurate planning and design of devices for treatment in confined spaces such as interstitial or intracavitary treatments close to bone structures. The method supports previous work in which undesired temperature increments outside of target regions and close to bone interfaces were detected (Burtnyk et al. 2010).

The method used to perform the hydrophone measurements was designed to enable the detection of the forward and the reflected waves independently as well as their interaction. For this, the hydrophone was placed perpendicular to the wave propagation direction so that it could be moved with a robotic arm between the transducer and the sample and obtain planar scans. The size and directivity of the hydrophone were selected in such a way that the setting would enable the acquisition without loss of information. The scanned region was chosen to be on the pre focal area of the acoustic field,

where the cross-section of the acoustic preasure beam is narrow. The dimensions of the scanned area were restricted mainly by the degrees of freedom and size of the mechanical components of the setup. So far, other authors have compared the results of their simulations against simulation results from other methods (Vyas & Christensen 2008, Zeng & McGough 2008). The method proposed here to perform hydrophone measurements allows the direct validation of numerical methods against experimental data, which is challenging when studying the acoustic field close to solid interfaces due to the hydrophone positioning.

For the hydrophone measurements, water was chosen as fluid transmission medium because most tissues in the body have similar acoustic properties except for fat, air and bone (ter Haar & Coussios 2007). Acrylic was chosen because of its well known acoustic properties and flexibility to create the setup. Even though the objective of this experiment was to study a simple interface, the properties of the selected materials are not exactly those of tissue and the acoustic field is expected to differ accordingly.

The highest error in the hydrophone measurements was obtained for a 5° incidence angle. This error is probably due to high amounts of noise in the measurement and is unlikely to be linked with the inherent physical phenomenon which is being modeled by the simulations.

The thermometry results for the simulated transducer showed that increments in temperature close to the boundary start when the distance between the target region and the solid interface is approximately 10 mm which corresponds to figure 5.3 g, h and i. This is consistent with bone heating (around 40°C) reported in (Burtnyk et al. 2010). This can be explained by high pressure of the forward wave located at the boundary. When this high pressure at the boundary is combined with a reflected wave, the final temperature in-

crement becomes important. This means that overheating of the tissue close to the bone can be minimized if it is ensured that the transducer is operated in such a way that the forward acoustic field presents low pressure close to the solid interface, which can be achieved using a multi-element transducer with various frequencies.

The results of the validation using MRI thermometry show that taking into account the reflections generated at the boundary is important to attain a better prediction of the heating pattern generated by the transducer when operating close to the bone. This increment can be related to the combination of a side lobe of the forward acoustic field with the reflected wave generated at the interface. These complex interactions of side lobes at the boundaries can be accounted for using the proposed model when designing a device or planning a treatment, while they can be easily overseen with more traditional approaches. During these experiments only incident angles close to 90° were present due to the circular nature of the boundary. Future experiments could be developed to study the effect of complex-angled interfaces.

The transmitted wave which propagates beyond the interface into the solid is absorbed quickly, heating the material. This will lead to heat propagation into nearby tissue. Proper simulation of this effect, combined with the method proposed in this paper may lead to a more accurate prediction of the temperature variations close to solid interfaces.

The method described in this work is based on a modified version of the Rayleigh-Sommerfeld integral. This numerical version has been implemented to take advantage of the high performance computation capabilities of graphic cards. Even when the natural complexity of the algorithm is $\mathcal{O}(n \times m)$ (where n is the number of points which constitute the acoustic source and m is the number of points within the volume), it is highly par-

allelizable and calculations could be performed on a graphics card, reducing the execution time by a factor of $\approx n/k$ where k is the number of processing cores in the graphic card.

This approach has the advantage of allowing for calculations on complexly shaped propagation media to model homogeneous acoustic wave propagation, such as it has been implemented using finite element methods, but with the advantage of reduced complexity of problem statement. Angular spectrum methods (ASM) have also been proven to be fast and accurate for homogeneous media calculations (Zeng & McGough 2008) and their extension, the hybrid angular spectrum (HAS), can be used for calculation within complex shapes and inhomogeneous media (Vyas & Christensen 2008). HAS propagates the pressure field from one plane to another, using always the result of one calculation as input for the next one. Further analysis of the capabilities of these techniques to simulate the effects of reflected waves close to bone interfaces will be useful to asses and compare their performance.

In this thesis we chose to validate the model using a clinical intraurethral device (Chopra et al. 2012) in order to ensure that it could be used in actual applications. However, this is a small applicator and the surface is small compared to other clinical applicators. Most of the interstitial HIU applicators would have this small size. However, if it was desired to use this model with larger devices, a high calculation speed can still be achieved by increasing the computational resources.

The validations performed in this study assert the accuracy of the proposed method to predict the thermal variation pattern generated in the studied scenarios. This model represents a valuable tool to understand and study the secondary effects that may appear in applications that deliver HIU close to bone interfaces.

Bibliography

Aubry, J. F., Tanter, M., Pernot, M., Thomas, J. L. & Fink, M. (2003), 'Experimental demonstration of noninvasive transskull adaptive focusing based on prior computed tomography scans', *The Journal of the Acoustical Society of America* **113**, 84.

Azhari, H. (2010), *Basics of Biomedical Ultrasound for Engineers*, Wiley-IEEE Press, United States of America.

Bao, S., Thrall, B. & Miller, D. L. (1997), 'Transfection of a reporter plasmid into cultured cells by sonoporation in vitro', *Ultrasound in Med. and Biol.* **23**(6), 953–959.

Bommannan, D., Okuyama, H., Stauffer, P. & Guy, R. H. (1992), 'Sonophoresis. i. the use of high-frequency ultrasound to enhance transdermal drug delivery', *Pharmaceutical Research* **9**(4), 559–564.

Brekhovskikh, L. M. & Godin, O. A. (1998), *Acoustics of Layered Media I.Plane and Quasi-Plane Waves*, Springer Series on Wave Phenomena, Springer, Berlin, Germany.

Bruneau, M. & Scelo, T. (2006), *Fundamentals of acoustics*, ISTE, Wiltshire, Great Britain.

Burtnyk, M. (2011), Conformal Heating of the Prostate for the Treatment of Localized Cancer using MRI-Guided Transurethral Ultrasound, PhD thesis, University of Toronto.

Burtnyk, M., Chopra, R. & Bronskill, M. (2010), 'Thermal analysis of the surrounding anatomy during 3-d mri-guided transurethral ultrasound prostate therapy', *AIP Conference Proceedings* **1215**, 251.

Canney, M. S., Souchon, R., Carpentier, A., Girard, F., Chapelon, J. & Lafon, C. (2010), 'Design and testing of an interstitial therapeutic ultrasound applicator for the thermal ablation of cerebral tumors', *J. Acoust. Soc. Am.* **128**(4), 2416–2416.

Chopra, R., Baker, N., Choy, V., Boyes, A., Tang, K., Bradwell, D. & Bronskill, M. J. (2008), '¡mri-compatible transurethral ultrasound system for the treatment of localized prostate cancer using rotational control.', *Med. Phys.* **35**(4), 1346–1357.

Chopra, R., Burtnyk, M., Baker, S. N., Choy, V., Lochhead, S. & Bronskill, M. J. (2004.), 'Feasibility of mri-guided transurethral thermal therapy for prostate cancer', *IEEE International Ultrasonics, Ferroelectrics and Frequency Control Joint 50th Anniversary Conference* **1**, 713–15.

Chopra, R., Colquhoun, A., Burtnyk, M., N'Djin, W. A., Kobelevskiy, I., Boyes, A., Siddiqui, K., Foster, H., Sugar, L., Haider, M. A., Bronskill, M. & Klotz, L. (2012), 'Mr imaging-controlled transurethral ultrasound therapy for conformal treatment of prostate tissue: initial feasibility in humans.', *Radiology* **265**(1), 303–13.

Chopra, R., Luginbuhl, C., Foster, F. S. & Bronskill, M. J. (2000), Wideband transducers for improved control of interstitial heating patterns, *in* 'Ultrasonics Symposium, 2000 IEEE', Vol. 2, pp. 1235–1238.

Cohen, M., Bartels, U., Branson, H., Kulkarni, A. V. & Hamilton, J. (2013), 'Trends in treatment and outcomes of pediatric craniopharyngioma', *Neuro-Oncology* p. 19752011.

Corporation, N. (n.d.), 'Cufft — nvidia developer zone', *https://developer.nvidia.com/cufft* .

Damadian, R. V. (1974), 'Apparatus and method for detecting'. US Patent 3,789,832.

Delabrousse, E., Salomir, R., Birer, A., Paquet, C., Mithieux, F., Chapelon, J.-Y., Cotton, F. & Lafon, C. (2010), 'Automatic temperature control for mr-guided interstitial ultrasound ablation in liver using a percutaneous applicator: Ex vivo and in vivo initial studies', *Magnet. Reson. Med.* **63**, 667679.

Diederich, C. J. (1996), 'Ultrasound applicators with integrated catheter-cooling for interstitial hyperthermia: theory and preliminary experiments', *Int. J. Hyperthermia* **12**(2), 279–297.

Diederich, C. J., Stafford, R. J., Nau, W. H., Burdette, E. C., Price, R. E. & Hazle, J. D. (2004), 'Transurethral ultrasound applicators with directional heating patterns for prostate thermal therapy: In vivo evaluation using magnetic resonance thermometry', *Med. Phys.* **31**(2), 405–413.

Graham, K. S. (1993), *Fundamentals of Mechanical Vibrations*, McGraw Hill, Inc, United States of America.

Hazle, J. D., Diederich, C. J., Kangasniemi, M., Price, R. E., Olsson, L. E. & Stafford, R. J. (2002), 'Mri-guided thermal therapy of transplanted tumors in the canine prostate using a directional transurethral ultrasound applicator', *Journal of Magnetic Resonance Imaging* **15**(4), 409–417.

Helmholtz, H. (1860), 'Theory of air oscillations in tubes with open ends', *Journal fur die Reine und Angewandte Mathematik* **57**, 1–72.

Hobson, D., Curiel, L., Chapelon, J. Y. & Pichardo, S. (2012), Dual-modality image guided high intensity focused ultrasound device design

for prostate cancer: A numerical study, *in* 'AIP Conference Proceedings', Vol. 1481, p. 131.

Huang, S. L., McPherson, D. D. & MacDonald, R. C. (2008), 'A method to co-encapsulate gas and drugs in liposomes for ultrasound-controlled drug delivery', *Ultrasound in Med. and Biol.* **34**(8), 1272–1280.

Hunt, J. W., Arditi, M. & Foster, F. S. (1983), 'Ultrasound transducers for pulse-echo medical imaging', *Biomedical Engineering, IEEE Transactions on* (8), 453–481.

Hydro, R. (2013), 'Soundspeed data for pipe materials and liquids, chemicals and water', Website. [Accessed 06 May 2013].
*http://www.rshydro.co.uk/sound-speeds.shtml

Hynynen, K. & Sun, J. (1999), 'Trans-skull ultrasound therapy:the feasibility of using image-derived skull thickness information to correct the phase distortion', *IEEE Trans. Ultrason. Ferroelectr. Freq. Control* **46**, 752755.

J H Wootton, P Prakash, I.-C. J. H. & Diederich, C. J. (2011), 'Implant strategies for endocervical and interstitial ultrasound hyperthermia adjunct to hdr brachytherapy for the treatment of cervical cancer', *Phys. Med. Biol.* **56**, 39673984.

Jaros, J., Treeby, B. E. & Rendell, A. P. (2012), Use of multiple gpus on shared memory multiprocessors for ultrasound propagation simulations, *in* '10th Australasian Symposium on Parallel and Distributed Computing, edited by J. Chen and R. Ranjan, ACS', Vol. 127, pp. 43–52.

Kikuchi, S., Saito, K., Takahashi, M. & Ito, K. (2007), 'Control of heating pattern for interstitial microwave hyperthermia by a coaxial-dipole antennaaiming at treatment of brain tumor', *Electronics and Communications in Japan (Part I: Communications)* **90**(12), 31–38.

Kinsey, A. M. & Diederich, C. J. (2008), 'Transurethral ultrasound applicators with dynamic multi-sector control for prostate thermal therapy: In vivo evaluation under mr guidance', *Med. Phys.* **35**(5), 20812093.

Kirchhoff, G. (1883), 'Towards a theory of light rays', *Annalen der Physik und Chemie* **18**, 663–695.

Kirk, D. B. & Hwu, W. W. (2010), *Programming Massively Parallel Processors*, Morgan Kaufmann, United States of America.

Kutter, O., Shams, R. & Navab, N. (2009*a*), 'Visualization and gpu-accelerated simulation of medical ultrasound from ct images', *Computer methods and programs in biomedicine* **94**(3), 250–266.

Kutter, O., Shams, R. & Navab, N. (2009*b*), 'Visualization and gpu-accelerated simulation of medical ultrasound from ct images', *Computer Methods and Programs in Biomedicine* **24**, 250–266.

Lafon, C., Chapelon, J. Y., Prat, F., Gorry, F., Margonari, J., Theillere, Y. & Cathignol, D. (1998), 'Design and preliminary results of an ultrasound applicator for interstitial thermal coagulation', *Ultrasound Med. Biol.* **24**(1), 113–122.

Lafon, C., Chavrier, F., Prat, F., Chapelon, J. Y. & Cathignol, D. (1999), 'Theoretical comparison of two interstitial ultrasound applicators designed to induce cylindrical zones of tissue ablation', *Med. Biol. Eng. Comput.* **37**, 298–303.

Lerch, R., Landes, H., Friedrich, W., Hebel, R., Hoss, A. & Kaarmann, H. (1992), Modelling of acoustic antennas with a combined finite-element-boundary-element-method, *in* 'Ultrasonics Symposium, 1992. Proceedings., IEEE 1992', pp. 581–584.

Lerch, R., Landes, H. & Kaarmann, H. T. (1994), Finite element modeling of the pulse-echo behavior of ultrasound transducers, *in* 'Ultrasonics Symposium, 1994. Proceedings., 1994 IEEE', Vol. 2, pp. 1021–1025.

Lynn, J. G., Zwemer, R. L., Chick, A. J. & Miller, A. E. (1942), 'A new method for the generation and use of focused ultrasound in experimental biology', *The journal of general physiology* **26**(2), 179.

McNamara, S. (2012), 'Treatment of primary brain tumours in adults', *Nursing Standard* **27**(14), 42–47.

Melodelima, D., Lafon, C., Prat, F., Theillere, Y., Arefiev, A. & Cathignol, D. (2003), 'Transesophageal ultrasound applicator for sector-based thermal ablation: First in vivo experiments', *Ultrasound in Med. and Biol.* **29**(2), 285–291.

Miller, D. L., Pislaru, S. V. & Greenleaf, J. F. (2002), 'Sonoporation: Mechanical dna delivery by ultrasonic cavitation', *Somatic Cell and Molecular Genetics* **27**(1/6), 115–134.

Miller, D. L., Smith, N. B., Bailey, M. R., Czarnota, G. J., Hynynen, K. & Makin, I. R. S. (2012), 'Overview of therapeutic ultrasound applications and safety considerations', *Ultrasound Med. Biol.* **31.4**, 623–634.

NDjin, W. A., Burtnyk, M., Kobelevskiy, I., Hadjis, S., Bronskill, M. & Chopra, R. (2012), 'Coagulation of human prostate volumes with mri-controlled transurethral ultrasound therapy: Results in gel phantoms', *Med. Phys.* **39**(7), 4524–4536.

Pan, H., Zhou, Y., Izadnegahdar, O., Cui, J. & Deng, C. X. (2005), 'Study of sonoporation dynamics affected by ultrasound duty cycle', *Ultrasound in Med. and Biol.* **31**(6), 849–856.

Parakka, M. J. (2013), 'Sonophoresis and nanotechnology- a review on the latest techniques in t.d.d.s', *International Journal of Current Pharmaceutical Research* **5**(2), 25–29.

Pennes, H. H. (1948), 'Analysis of tissue and arterial blood temperatures in resting human forearm', *J. Appl. Physiol.* **1**(2), 32–122.

Pichardo, S. & Hynynen, K. (2007), 'Treatment of near-skull brain tissue with a focused device using shear-mode conversion: a numerical study', *Phys. Med. Biol.* **52**, 73137332.

Pierce, A. D. (1994), *Acoustics. An introduction to its physical principles and applications*, The Acoustical Society of America, Melville, NY.

Piranda, B., Steichen, W. & Ballandras, S. (1998), 'Comparison between different finite element/boundary formulations for modeling acoustic radiation in fluids', *Proceedings of the Ultrasonics Symposium, 1998* **2**, 1073–1076.

R Chopra, M Burtnyk, M. A. H. & Bronskill, M. J. (2005.), 'Method for mri-guided conformal thermal therapy of prostate with planar transurethral ultrasound heating applicators', *Phys. Med. Biol* **50**, 49574975.

Reichl, T., Passenger, J., Acosta, O. & Salvado, O. (2009), Ultrasound goes gpu: real-time simulation using cuda, *in* 'SPIE Medical Imaging', International Society for Optics and Photonics, pp. 726116–726116.

Rieke, V. & Pauly, K. B. (2008), 'Mr thermometry', *Magn. Reson. Imaging* **27**(3), 376–390.

Ross, A. B., Diederich, C. J., Nau, W. H., Gill, H., Bouley, D. M., Daniel, B., Rieke, V., Butts, R. K. & Sommer, G. (2004), 'Highly directional transurethral ultrasound applicators with rotational control for mri-guided prostatic thermal therapy', *Phys. Med. Biol.* **49**, 189204.

Selfridge, A. R. (1985), 'Approximate material properties in isotropic materials', *IEEE Trans. Sonics Ultrason.* **SU-32**(3), 381–394.

Sheta, A. F., Elshafiey, I., Mohra, A., Siddiqui, Z. & Sebak, A. R. (2012), 'A compact antenna for microwave imaging and hyperthermia treatment of brain tumor', *Antenna Technology and Applied Electromagnetics (ANTEM), 2012 15th International Symposium on* pp. 1–4.

Siddiqui, K., Chopra, R., Vedula, S., Sugar, L., Haider, M., Boyes, A. & Klotz, L. (2010), 'Mri-guided transurethral ultrasound therapy of the prostate gland using real-time thermal mapping: initial studies', *Urology* **76**(6), 1506–1511.

Takahashi, Y., Kato, K., Tsuchiya, K., Yabuhara, T., Uzuka, T. & Takahashi, H. (2006), 'Design and construction of resonant cavity applicator for brain tumor hyperthermia treatment without contact', *Proceedings of the 28th IEEE EMBS Annual International Conference New York City, USA* pp. 4074–4077.

Tanter, M., Pernot, M., Aubry, J. F., Montaldo, G., Marquet, F. & Fink, M. (2007), 'Compensating for bone interfaces and respiratory motion in high-intensity focused ultrasound', *International Journal of Hyperthermia* **23**(2), 141–151.

ter Haar, G. & Coussios, C. (2007), 'High intensity focused ultrasound: physical principles and devices', *International Journal of Hyperthermia* **23**(2), 89–104.

Vuong, D., Rades, D., van Eck, A. T. C., Horstmann, G. A. & Busse, R. (2013), 'Comparing the cost-effectiveness of two brain metastasis treatment modalities from a payer's perspective: Stereotactic radiosurgery versus surgical resection', *Clinical Neurology and Neurosurgery* **115**(3), 276–284.

Vyas, U. & Christensen, D. (2008), 'Ultrasound beam propagation using the hybrid angular spectrum method', pp. 2526–2529.

Vyas, U. & Christensen, D. (2012), 'Ultrasound beam simulations in inhomogeneous tissue geometries using the hybrid angular spectrum method', *IEEE Trans. Ultrason. Ferroelectr. Freq. Control* **59**(6), 1093–1100.

Walker, D. A., Liu, J., Kieran, M., Jabado, N., Picton, S., Packer, R. & Rose, C. S. (2013), 'A multi-disciplinary consensus statement concerning surgical approaches to low-grade, high-grade astrocytomas and diffuse intrinsic pontine gliomas in childhood (cpn paris 2011) using the delphi method', *Neuro-Oncology* .

Wein, W., Brunke, S., Khamene, A., Callstrom, M. R. & Navab, N. (2008), 'Automatic ct-ultrasound registration for diagnostic imaging and image-guided intervention', *Medical image analysis* **12**(5), 577–585.

Wu, P. & Stepinski, T. (1999), 'Extension of the angular spectrum approach to curved radiators', *J. Acoust. Soc. Am.* **105**(5).

Yin, X., Epstein, L. M. & Hynynen, K. (2006), 'Noninvasive transesophageal cardiac thermal ablation using a 2-d focused, ultrasound phased array: A simulation study', *IEEE Trans. Ultrason. Ferroelectr. Freq. Control* **53**(6), 1138–1149.

Zeng, X. & McGough, R. (2008), 'Evaluation of the angular spectrum approach for simulations of nearfield pressures', *J. Acoust. Soc. Am.* **123**(1), 68–76.